Chinese Chemical Letters 33 (2022) 1154–1168

Contents lists available at ScienceDirect

Chinese Chemical Letters

journal homepage: www.elsevier.com/locate/cclet

Nanostructured materials with localized surface plasmon resonance for photocatalysis

Juan Li[a], Zaizhu Lou[a,b,*], Baojun Li[a]

[a] Institute of Nanophotonics, Jinan University, Guangzhou 511443, China
[b] State Key Laboratory for Crystal Materials, Shandong University, Ji'nan 250100, China

ARTICLE INFO

Article history:
Received 21 April 2021
Revised 6 June 2021
Accepted 25 July 2021
Available online 31 July 2021

Keywords:
Localized surface plasmon resonance
Plasmonic photocatalysis
Plasmonic semiconductor
Hot electrons
Solar energy harvesting

ABSTRACT

Localized surface plasmon resonance (LSPR) enhanced photocatalysis has fascinated much interest and considerable efforts have been devoted toward the development of plasmonic photocatalysts. In the past decades, noble metal nanoparticles (Au and Ag) with LSPR feature have found wide applications in solar energy conversion. Numerous metal-based photocatalysts have been proposed including metal/semiconductor heterostructures and plasmonic bimetallic or multimetallic nanostructures. However, high cost and scarce reserve of noble metals largely limit their further practical use, which drives the focus gradually shift to low-cost and abundant nonmetallic nanostructures. Recently, various heavily doped semiconductors (such as WO_{3-x}, MoO_{3-x}, $Cu_{2-x}S$, TiN) have emerged as potential alternatives to costly noble metals for efficient photocatalysis due to their strong LSPR property in visible-near infrared region. This review starts with a brief introduction to LSPR property and LSPR-enhanced photocatalysis, the following highlights recent advances of plasmonic photocatalysts from noble metal to semiconductor-based plasmonic nanostructures. Their synthesis methods and promising applicability in plasmon-driven photocatalytic reactions such as water splitting, CO_2 reduction and pollution decomposition are also summarized in details. This review is expected to give guidelines for exploring more efficient plasmonic systems and provide a perspective on development of plasmonic photocatalysis.

1. Introduction

Evoked by present dilemma of energy shortage and environmental pollution, developing renewable energy is highly urgent. Solar energy as one of "green" energy resources has attracted worldwide attention, but its efficient utilization is a significant challenge. Photocatalysis, an emerging "green technology", can convert solar energy to chemical fuels to address current global environmental and energy crisis [1–3]. Since the discovery of Honda-Fujishima effect on TiO_2 photoelectrode in 1972 [4], semiconductor photocatalysis has dominated the research area for several decades [5–7]. However, intrinsic wide band gaps (>3.1 eV) render the conventional semiconductors (TiO_2, ZnO) solely responsive to ultraviolet (UV) light, accounting for only 4% of solar energy. Other visible-light responsive semiconductors like α-Fe_2O_3, are inherited with short charge-carrier diffusion lengths and suffer from poor charge separation efficiency, significantly hampering their applications in photocatalysis [8]. In order to enhance the photoactivities of semiconductors, various methods have been proposed, such as doping external elements to tune their band structures for a broad optical response [9,10], constructing suitable heterostructure to retard the charge recombination [11,12], engineering surface architectures for more active sites [13,14] *etc.* Nevertheless, weak photoresponse and low quantum efficiency are still two major bottlenecks for large-scale application of semiconductor photocatalysts.

Along with semiconductor photocatalysis, localized surface plasmon resonance (LSPR) mediated photocatalysis has fascinated much attention in solar energy conversion [15–19]. LSPR is one physical phenomenon of free electrons oscillation of with incident photons confined on noble metallic nanoparticles (NPs) surface. Plasmonic metallic NPs (Au, Ag) were initially used to sensitize semiconductors and improve their photoelectric response by constructing noble metal/semiconductor hybrids [20–22]. Owing to LSPR effect, plasmonic NPs can transfer solar energy to adjacent semiconductors to drive chemical reactions. Intriguingly, apart from acting as light absorber, plasmonic NPs themselves can also serve as active sites to directly induce catalysis. Plasmon-induced active hot charge carriers, electrons and holes can drive surface

---

[*] Corresponding author at: Institute of Nanophotonics, Jinan University, Guangzhou 511443, China.
E-mail address: zzlou@jnu.edu.cn (Z. Lou).

https://doi.org/10.1016/j.cclet.2021.07.059
1001-8417/

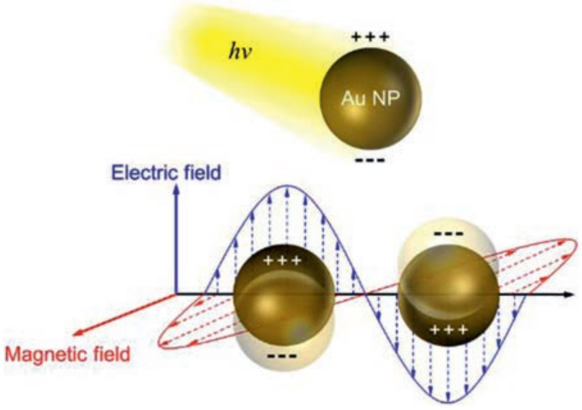

Fig. 1. Schematic illustration of LSPR excitation on metallic NPs.

catalytic reaction and modulate the reaction path [23–26]. LSPR excitation induces strong light harvesting, hot electron generation and localized heating effect, all of which could be beneficial for photochemical reactions [27–30]. Although plasmonic noble metals exhibit favorable advantages over traditional semiconductors, high cost and scarce reserve significantly inhibit their practical applications in photocatalysis. Moreover, LSPR of noble metallic NPs mostly localize in visible light region and near-infrared light accounting for more than 50% of solar energy failed to be well-utilized. Note that non-noble metals like Al and Cu also exhibit LSPR properties, which are considered as strong competitors to noble metals in term of their optical response. While both Al and Cu are cost-effective, their wide applicability for photocatalysis is largely hindered by the instability under ambient conditions. For example, Al has an inherent tendency to form oxides upon exposure to air due to high reduction potential (1.66 V). Cu NPs are also prone to oxidation and lead to the formation of Cu_2O or CuO.

Developing nonmetallic plasmonic nanostructures that enable broad-spectrum solar harvesting as potential substitutes of noble metals is of significance to sustainable and energy-efficient plasmonic photocatalysis. Recently, various semiconductors with heavy doping (WO_{3-x}, $Cu_{2-x}S$, MoO_{3-x}, *etc.*) have emerged as a burgeoning research hotspot due to their strong LSPR absorption in visible-near infrared (vis-NIR) region [31–38]. There has been debate as to whether defect absorption or SPR is responsible for strong absorption of heavily-doped semiconductors. Alivisatos and Manthiram theoretically proved that the intense absorption of WO_{3-x} is arised from the unique property of their outer-*d* valence electrons, providing theoretical support for non-metallic LSPR effect [39]. Since then, numerous nonmetallic plasmonic nanostructures have springed up as active photocatalysts and opened a new route for the development of photocatalysis [40–45]. In this review, we introduce recent advances of plasmonic photocatalysts from noble metal to semiconductor-based plasmonic nanostructures and further discuss their characterization and photocatalytic applications (water splitting, artificial photosynthesis, pollution decomposition *etc.*) in detail. Finally, we also present an outlook for the development of plasmonic photocatalysts and provide guidelines for optimizing the existing plasmonic systems.

2. Localized surface plasmon resonance

2.1. LSPR property

LSPR is an intriguing phenomenon associated with collective oscillations of free electrons with incident light Fig. 1). The extent of interaction between materials and light can be described by a complex dielectric function based on the Drude-Lorentz model as follows (Eqs. 1–4):

$$\varepsilon_p(\omega) = \varepsilon_r(\omega) + \varepsilon_i(\omega) \tag{1}$$

$$\varepsilon_r(\omega) = \varepsilon_\infty - \frac{\omega_p^2}{\omega^2 + \gamma^2} \tag{2}$$

$$\varepsilon_i(\omega) = \frac{\omega_p^2 \cdot \gamma}{\omega\left(\omega + \gamma^2\right)} \tag{3}$$

$$\omega_p = \sqrt{\frac{Ne^2}{m_e \varepsilon_0}} \tag{4}$$

where ε_p is dielectric function of materials, ε_r and ε_i are real and imaginary parts, respectively. ε_∞ is the high frequency dielectric constant of materials, ω_p is plasma frequency, ω is light frequency, γ is the damping constant that represents free carriers scattering, N is free carriers density, m_e is the effective mass of free carriers, e is elementary charge and ε_0 is the permittivity of vacuum. ε_r is determined by electric field induced polarization, whereas ε_i basically corresponds to damping and energy loss upon absorption at NPs surface [46]. As light irradiates on metallic NPs (Au, Ag, Cu), the associated electric field induces polarization of electrons density to one surface. At plasmon wavelength, electrons on NPs surface occur resonant oscillation to exhibit a strong LSPR absorption [47–49].

The LSPR wavelength of metallic NPs largely depends on the metal nature, morphology and dielectric constants of the surrounding media (Fig. 2). For example, by varying the geometry of Ag NPs from spheres to wires or cubes, both LSPR modes and wavelength are changed [18]. Moreover, LSPR wavelength also changes with the surrounding media due to variation in dielectric constant. The LSPR wavelengths of Ag nanocubes were found to red shift as the surrounding refractive index of solvents increased [50]. The longitudinal plasmon wavelength of Au nanorods (NRs) exhibits a nearly linear relation with aspect ratio as well as refractive index of surrounding solvents [47,51]. By tailoring these parameters, the corresponding photoresponse of metallic NPs can be finely manipulated, which is expected to improve the solar utilization.

The LSPR phenomenon is not restricted to metallic NPs and could also be observed in semiconductors with high free carrier density. Similar to noble metals, LSPR in semiconductors are originated from resonant interaction of free carriers and incident light, as described by the complex dielectric function. However, unlike metals, LSPR in semiconductors can be induced by free electrons or holes depending on the dopant nature, which are labeled as n-type or p-type plasmonic semiconductors, respectively [52]. Besides, LSPR wavelength in semiconductors is largely up to free carrier density. Luther et al. investigated the effect of free carrier density on LSPR frequency (wavelength). For NPs size in the range of 2–12 nm, carrier density of 10^{19}–10^{22} cm^{-3} generates LSPR in infrared range while carrier density below 10^{19} cm^{-3} is too low to support one LSPR mode [32]. Due to lower carrier density in comparison to noble metals, semiconductors usually exhibit LSPR in broad Vis-NIR region. For example, p-type self-doped copper chalcogenide ($Cu_{2-x}X$, X = S, Se, Te) nanocrystals (NCs) exhibit LSPR absorption in NIR region generated by free holes oscillation (Figs. 3a–c) [53]. Control over dopant type and extent can impact the free carrier density, leading to different LSPR energies and spectral shapes within the same host material. Fang *et al.* reported that for the same doping level, LSPR is at lower energy and has a smaller bandwidth for Ti-doped than Sb-doped In_2O_3 NCs, indicating lower free carrier density due to the formation of deep defect states within Ti:In_2O_3 band gap [54]. Similar phenomena have been widely reported across several metal oxides. The plasmonic behavior of $Cu_{2-x}S$ NCs also can be tuned *via* changing the

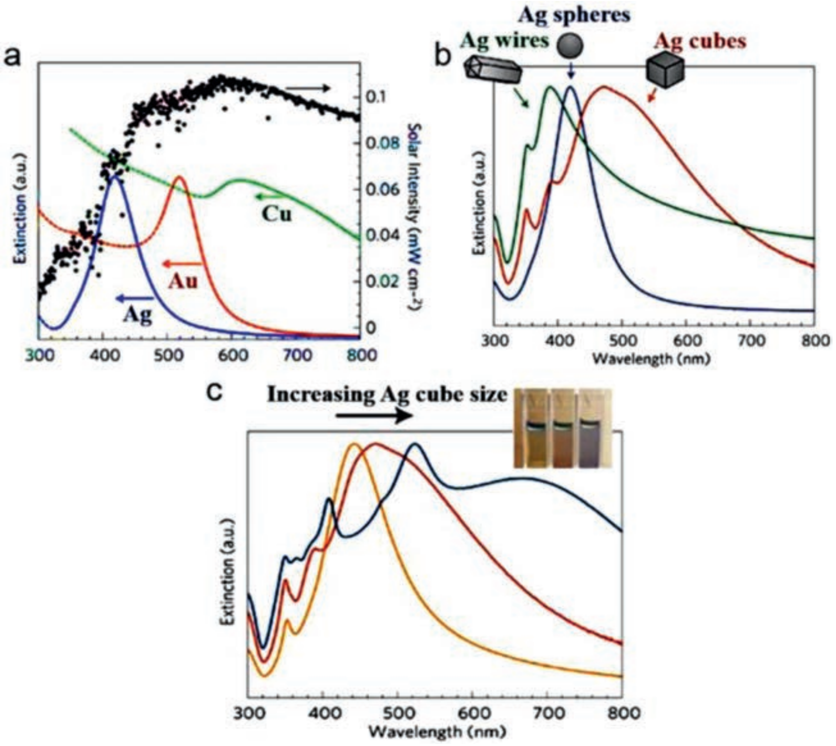

Fig. 2. The plasmonic resonant wavelength dependence of metallic NPs on their (a) metal species, morphology of (b) shape and (c) size. Reproduced with permission [18]. Copyright 2011, Nature Publishing Group.

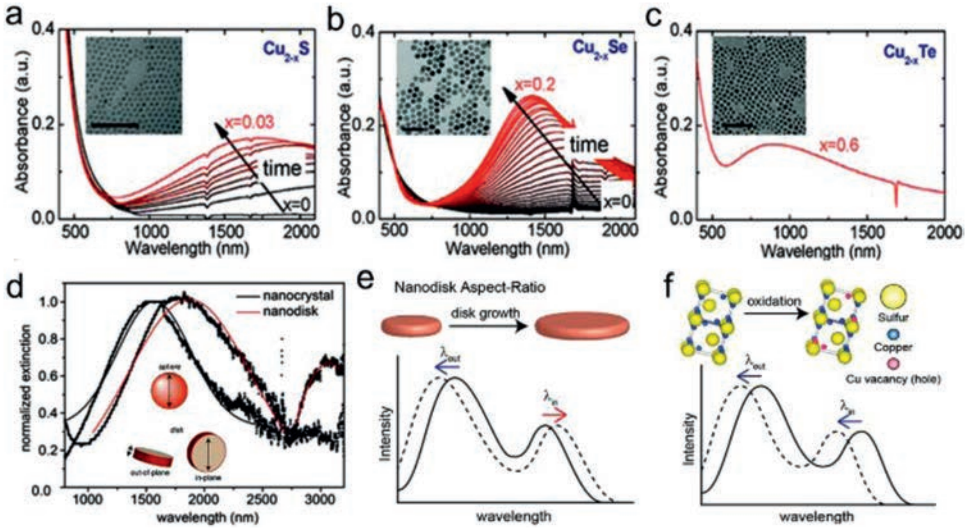

Fig. 3. (a–c) Extinction spectra and TEM images of $Cu_{2-x}S$ (x = 0–0.03, a), $Cu_{2-x}Se$ (x = 0–0.2, b) and $Cu_{2-x}Te$ (x = 0.6, c) NCs. Reproduced with permission [53]. Copyright 2011, American Chemical Society. (d) Shape-dependent extinction spectra of $Cu_{2-x}S$ NCs with sphere and nanodisks. Reproduced with permission [33]. Copyright 2011, American Chemical Society. The LSPR dependence of $Cu_{2-x}S$ nanodisks on (e) aspect ratio and (f) free carrier density. Reproduced with permission [57]. Copyright 2012, American Chemical Society.

composition with different Cu^+ doping extent. By a versatile post-synthesis reaction, the Cu/S ratio in NCs could be gradually increased from 1.1:1 to 2:1 while preserving their size and morphology. With increasing incorporation of Cu, the LSPR band of covellite $Cu_{2-x}S$ NCs red-shifted and decreased in intensity until it vanished for NCs with Cu_2S composition. It is mainly attributed to the decrease of free carrier density in NCs due to the increase in Cu stoichiometry [55]. A similar red shift and an increase in full-width at half maximum of LSPR band were also observed with increasing of Cu/S feed ratios, ascribing to the change of free carriers density induced by phase transformation [56]. In addition to free carrier density modulation, the shape parameters and crystal structure also greatly influence the LSPR of semiconductor NCs. The $Cu_{2-x}X$ exhibits a diverse crystal phases and morphology, which have a huge impact on their plasmonic response. The djurleite $Cu_{1.94}S$ nanodisks display two LSPR peaks in NIR and Mid-IR regions, while both roxbyite $Cu_{1.8}S$ and covellite CuS have only one peak in NIR region [33] (Fig. 3d). $Cu_{2-x}S$ nanodisks have two planes labeled as "in-plane" and "out-of-plane", where each plane corresponds to one LSPR mode. The characteristic LSPR wavelengths vary with the aspect ratio (diameter *vs.* thickness) and carrier density of nanodisks [57]. Increasing the aspect ratio induces out-of-

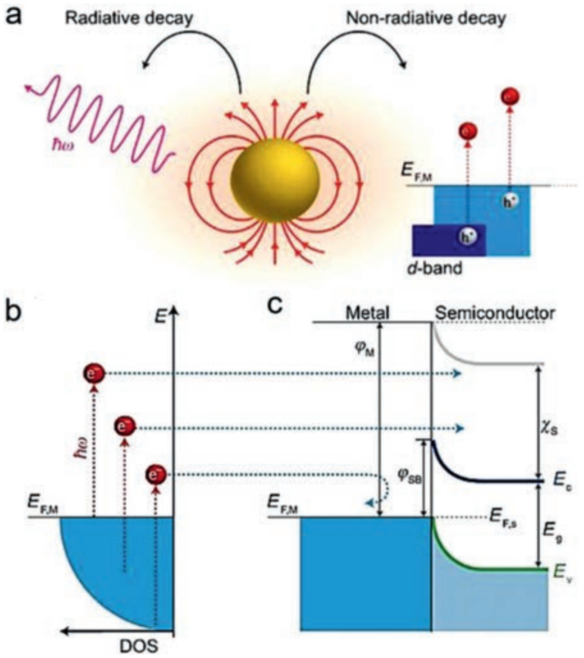

Fig. 4. (a) LSPR undergo decay by either radiative photons emission or nonradiative relaxation to generate hot electrons. (b) Hot electrons with a wide distribution range in energy. (c) Hot electrons with large energy can be injected to CB of adjacent semiconductors. Reproduced with permission [58]. Copyright 2011, Nature Publishing Group.

plane plasmon to blue-shift and in-plane to red-shift, consistent well with Mie scattering theory (Fig. 3e). As only hole carrier density is increased, both out-of-plane and in-plane plasmon are expected to blue-shift according to Drude theory (Fig. 3f). These results above indicate that both morphology (size, shape, aspect ratio *etc.*) and the free-carriers density (related to composition and phase) should be carefully considered to achieve dynamic tailoring for LSPR characteristics of semiconductor NCs.

2.2. LSPR-enhanced photocatalysis

The LSPR enables significant electric field enhancement on metallic NPs surface, known as near-field enhancement, which is beneficial for efficient light absorption and charge-carrier generation [58–60]. This near-field enhancement attenuates exponentially with the distance away from metal NPs surface and spatially limited to nanoscale “hot spots” region around the surface. The excited LSPR undergo decay by either radiative photons emission or nonradiative relaxation (Fig. 4), and the latter forms the basis of photocatalytic applications. The hot electrons are generated during the nonradiative decay through intra- or inter-band electrons transition. For Au and Ag NPs, owing to their fairly low-lying *d*-band below Fermi level, hot electrons generate primarily via intraband transitions within conduction band (CB) and the energies exhibit a wide distribution range of 1–4 eV [18,59,61]. Ultrafast measurements have shown that these hot electrons rapidly thermalize in isolated NPs, and the lifetime is extremely short in the range of 1–100 ps [58]. However, as metallic NPs are married with semiconductors, hot electrons with sufficient energy can be injected to CB of adjacent semiconductors across interfacial Schottky barrier to impede the decay, greatly altering their dynamics [59,62,63]. Similar to conventional electron transfer, hot electron injection is manipulated by the heterostructural interfacial contact and band alignment [25,59,64,65]. Therefore, elaborate structural engineering is highly needed for a fast hot electron injection to avoid the decay. For plasmonic semiconductors, LSPR-excited hot carriers (electrons or holes) also exhibit a similar ultrafast dynamic with that of metallic NPs.

During plasmonic photocatalytic process, plasmon-induced hot electrons can be transferred to adjacent semiconductor or directly interact with molecules adsorbed on plasmonic NPs surface [24,66–68]. The extracted hot electrons can activate specific chemical bonds of reactants and modify the reaction pathway, making a big difference to products selectivity [69]. Besides, hot electrons enable accelerated desorption of certain surface-adsorbed species, further promoting the catalytic activity and simultaneously prolong the stability of plasmonic NPs [70]. The hot electrons have been demonstrated to play dominant role in various plasmon-enhanced chemical reactions including CO_2 reduction [71–73], H_2 evolution [74–76] *etc.* However, compared to widely studied photochemistry driven by hot electrons, the ones that driven by plasmonic hot holes have received less attention, probably due to much shorter lifetime of hot holes than hot electrons [77]. The hot carriers that do not participate in reaction could subsequently dissipate their energy to lattice phonon *via* electron-phonon scattering, inducing considerable photothermal effect (heating), which is also favorable for chemical conversion since both reaction rates and routes are closely related to temperature [78–81]. The photothermal heating is an effective driving force to accelerate the reaction by promoting the adsorption-desorption of surface adsorbent and shifting chemical equilibria toward higher products yield [82,83]. In plasmonic photocatalysis, by structural design of plasmonic catalysts, hot carrier driven reactant activation and photothermal effect could coexist and synergistically make positive contributions to enhance plasmonic catalytic efficiency [84–87].

The electric near-field enhancement, plasmonic hot carriers and thermal effect are representative features of LSPR, which are mostly investigated in plasmonic photocatalysis and offer guidelines for developing efficient photocatalysts. To date, based on these plasmonic effects, various plasmonic nanostructures have been reported as active photocatalysts and herein is primarily divided into two big categories of noble metal-based and nonmetallic plasmonic photocatalysts according to the components. The synthesis, LSPR property and photocatalytic applications of these photocatalysts are discussed in details below.

3. Noble metal based plasmonic photocatalysts

3.1. Metal-semiconductor composites as plasmonic photocatalysts

For conventional semiconductor photocatalysts, narrow photoresponse range and low quantum efficiency are two major challenges for their practical applications. The controlled integration of semiconductor with plasmonic noble metals (Au, Ag) has been considered as an effective route to improve the situation. In 2008, Awazu group deposited TiO_2 on Ag/SiO_2 core-shell structures and initially proposed the concept of “plasmonic photocatalysis”. The enhanced electric field on Ag NPs surface was pioneered to afford better photocatalytic performance for decomposition of methylene blue (MB) [20]. The same year, Huang group proposed a stable plasmonic photocatalyst of Ag@AgCl with strong absorption in visible region for efficient degradation of organic dyes [21]. Compared with spherical NPs with only one LSPR mode, anisotropic metallic NPs with multipolar LSPR modes could achieve broader vis-NIR light harvesting. Liu *et al.* prepared Au NRs loaded TiO_2 phototcatalysts and found that both transversal and longitudinal plasma of Au NRs (with tunable adsorption from 630 nm to 810 nm) could induce photocatalytic 2-propanol oxidation [88]. The adjustable light adsorption caused by tunability of Au NRs aspect ratio is benefit to developing photocatalyst with specific light harvesting. Moreover, Au NRs and metal NPs (Au, Ag or Pt) co-decorated CdS nanowires (NWs) ensemble with tunable and progressive harvesting of vis-

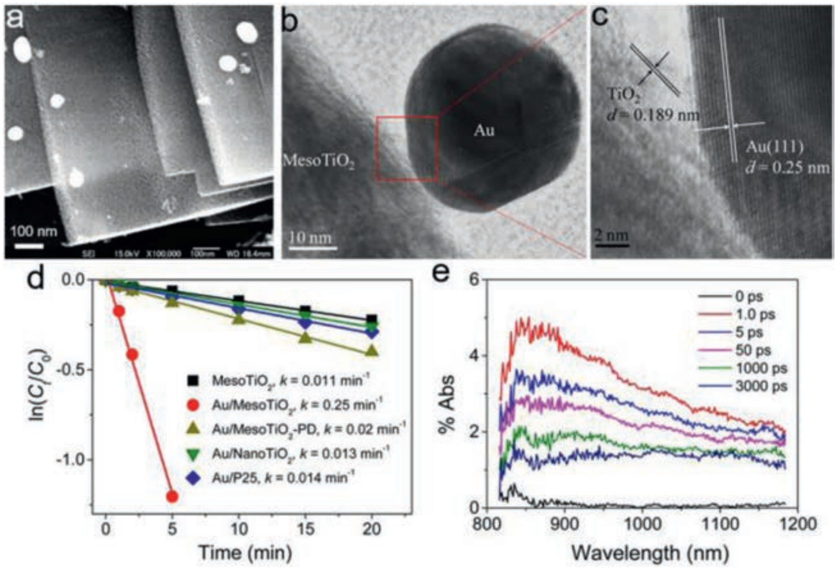

Fig. 5. (a) SEM images and (b, c) HRTEM images of Au/MesoTiO$_2$. (d) Kinetic linear fitting curves for photocatalytic MB degradation over different samples under 460–700 nm light irradiation. (e) Time-resolved DRS observed after 530 nm laser flash photolysis of Au/MesoTiO$_2$. Reproduced with permission [90]. Copyright 2013, American Chemical Society.

NIR light ($\lambda > 570$ nm) has also been reported for distinctly boosting photoreduction of 4-nitroaniline and water splitting to H_2 [89]. The results show that finely progressive control over a series of factors, including interfacial interaction, morphology optimization and cocatalyst addition in metal-semiconductor (Au NRs-CdS) heterostructures, can lead to tunable and improved performance for vis-NIR driven plasmonic photocatalysis.

In plasmonic metal-semiconductor photocatalyst, plasmon-induced hot electrons can be injected into CB of nearby semiconductors across interfacial Schottky barriers, dominantly driving the photocatalytic redox reaction. Bian *et al.* successfully deposited Au NPs on TiO_2 mesocrystals by a simple impregnation method (Fig. 5) [90]. The diffuse reflectance spectroscopy (DRS) measurements demonstrate that LSPR-induced hot electrons are injected from Au NPs to TiO_2 mesocrystals, directionally migrate from basal surfaces to the edges of plate-like TiO_2 nanocrystal. Such anisotropic electron flow significantly retarded the charge recombination of hot carriers in Au NPs, thereby improving visible-light driven photocatalytic organic-pollutant degradation.

Plasmon-induced hot electron injection in metal-semiconductor system provides a promising avenue to improve the efficiency of photocatalysis. To this end, the metal-semiconductor interface is of significance and should be elaborately engineered to facilitate rapid hot electron injection that is competitive with ultrafast hot electron relaxation. Apart from surface decoration, core-shell geometry is favorable in view of its maximized contact and optimal configuration for efficient charge transfer. Yadong Li group produced core-shell structures of Au@MS (M = Cd, Zn) with controllable shapes and unique atomically organized interfaces *via* aqueous cation exchange-facilitated nonepitaxial growth. Beneficial from interfacial- and structural-optimization, Au@MS enables improved hot electron injection with an estimated quantum yield of ~48% for boosting plasmon-enhanced photocatalytic H_2 evolution [74]. Recently, various Au NR@ZnO core-shell photocatalysts with tunable shell thickness were also successfully prepared to achieve solar-driven CO_2 conversion to CH_4, further demonstrating the redox reactivity of plasmonic hot electrons. With ZnO shell acting as electron acceptor, the hot electrons prolonged the lifetime, which are more conducive to being captured by absorbed molecules to participate in the reaction. Both of Au core and ZnO shell are co-excited by solar light, synergistically contributing to significant enhancement of CO_2 photoreduction [91].

The coupling manners between metal and semiconductor are also crucial for photocatalytic performance of plasmonic metal-semiconductor photocatalysts. Instead of depositing metallic NPs onto semiconductor, anisotropic growth of semiconductor onto Au NPs afford better interfacial contact between them. Besides, anisotropic metallic NPs with high-curvature sites such as nanocubes corners and nanocones tips, are found to be locations for maximum electric field distribution compared with spherical NPs [92]. Because of the lightning rod effect and decreased radiative damping, anisotropic metallic NPs with high-curvature sites concentrate the incident energy and largely facilitate plasmonic hot electrons generation and transfer, which play significant roles for activating surface chemical reaction [93]. Therefore, controlled selective overgrowth of semiconductors at high-curvature sites of metallic NPs is valid strategy to obtain active plasmonic photocatalysts. Au triangular nanoprisms (Au TNPs) with unique anisotropic structures and multipolar LSPR modes, offer diverse sites of corner, edge and surface for coupling with semiconductors to construct various plasmonic photocatalysts. Lou et al. constructed anisotropic Ag_2S-edged Au TNPs by controlling preferential overgrowth (Fig. 6). Under vis-NIR light irradiation, Ag_2S-edged Au TNPs achieve maximum H_2 generation rate (796 μmol h^{-1} g^{-1}), almost four times higher than those of Ag_2S-covered Au TNPs (216 μmol h^{-1} g^{-1}) and pure Au TNPs (none). Single-particle photoluminescence (PL) measurements have been performed and an obvious PL quenching in Ag_2S-edged Au TNPs demonstrates SPR-induced hot electron transfer from Au-TNPs to Ag_2S for boosting H_2 generation [75]. Plasmonic hot electrons have been demonstrated to play a vital role in photocatalysis. However, only a few hot electrons with high energy can cross the as-formed Schottky barrier between metal and semiconductor for photocatalysis. The photocatalytic efficiency of plasmonic metal-semiconductor heterostructure is still challenged by slow charge mobility, inefficient hot electrons utilization and lack of active sites for redox reactions.

3.2. Bimetallic/multimetallic composites as plasmonic photocatalysts

Due to fast electrons transfer between metallic parts, bimetallic/multimetallic NPs are expected to show unique performance in

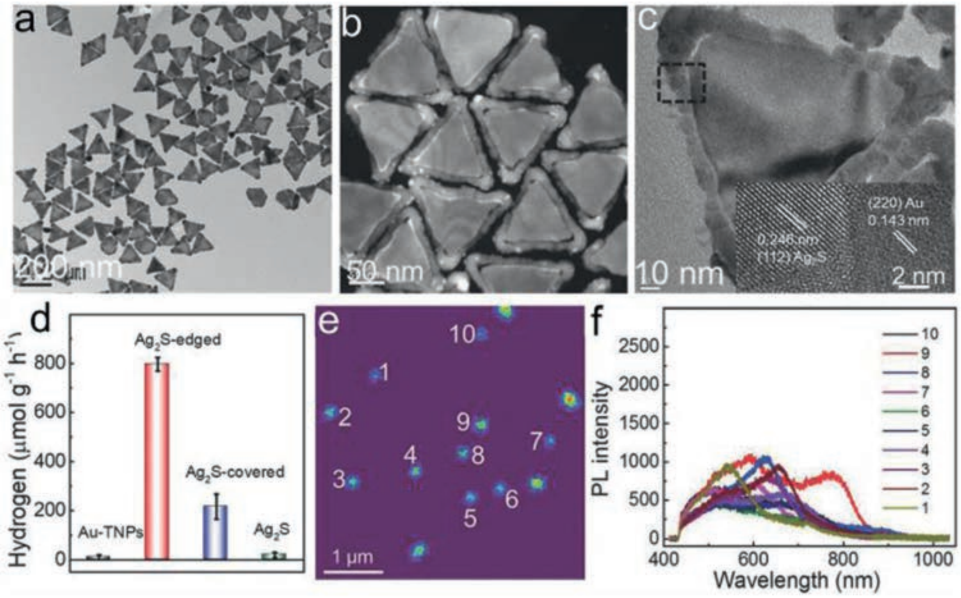

Fig. 6. (a) TEM, (b) High-angle annular dark-field scanning TEM and (c) HRTEM images of Ag_2S-edged Au TNPs. (d) Average H_2 generation rates over Ag_2S-covered, Ag_2S-edged, pure Au TNPs and Ag_2S photocatalysts under Vis-NIR light irradiation. (e, f) Single-particle PL image and spectra of Ag_2S-edged Au TNPs. Reproduced with permission [75]. Copyright 2018, Wiley-VCH.

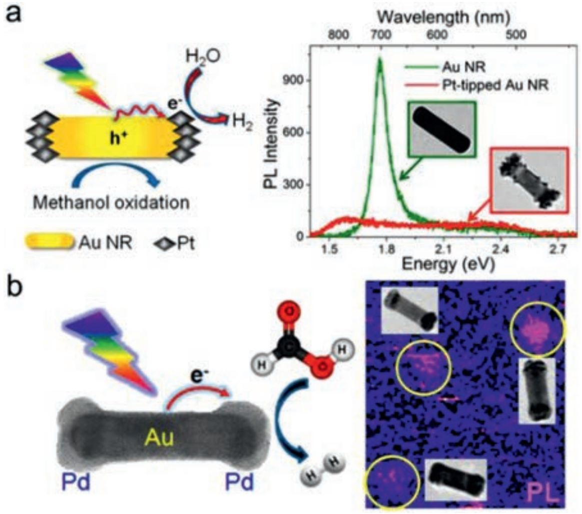

Fig. 7. Single-particle PL study of (a) Pt-tipped Au NRs for plasmon-enhanced water splitting and (b) Pd-tipped Au NRs for plasmon-enhanced HCOOH dehydrogenation. Reproduced with permission [94,95]. Copyright 2014, American Chemical Society.

photocatalysis. Various bimetallic NPs with enhanced charge separation have been developed, including Au-Pt, Au-Pd, Au-Cu, *etc.* [94–97]. In order to achieve efficient light utilization and high catalytic activity simultaneously, the intimate integration of plasmonic and catalytic metals is strongly desirable [98]. Majima group developed anisotropic Pt/Pd-tipped Au NRs, which simultaneously act as light absorber and catalytic active site to boost H_2 evolution from water splitting [94] and formic acid dehydrogenation [95], respectively (Fig. 7). Both PL quenching and light scattering from single Pt/Pd-tipped Au NRs confirmed hot electron transfer from excited Au to Pt/Pd. To further promote generation and transfer of hot electrons, Tang *et al.* reported freestanding heterosuperstructures of Au NRs@Pd (Au@Pd SSs), where ordered Pd nanoarrays are precisely grown on AuNRs surfaces *via* seed-mediated approach. With help of strong antenna effect in ordered Pd nanoarrays, plasmonic AuNRs engender abundant hot electrons to promote molecular oxygen activation; while vertical organization of Pd on Au NRs with small contact not only exposes rich active sites for reactants but also prolongs hot electron lifetime, largely enhancing C—C coupling reaction [99].

Apart from 1D NRs, 2D Au TNPs are also promising components for bimetallic plasmonic photocatalysis, which have multiple SPR modes including in-plane dipole SPR (DSPR), multipole SPR (MSPR) and out-of-plane SPR in visible-NIR region. Lou *et al.* synthesized three types of anisotropic Pt-covered, Pt-edged, and Pt-tipped Au TNPs by seed and subsequently controlling overgrowth, as shown in Figs. 8a–f. With intense electric field and more interface contact, Pt-edged Au TNPs facilitates hot electron transfer, leading to superior photocatalytic activity for H_2 generation than the other two. By single-particle PL spectra, in-plane DSPR mode of Au TNPs was demonstrated as the dominant channel for hot electrons transfer to edged Pt [100]. By *in situ* etching of single Au TNP, 2D Au obtuse TNP (O-TNP) and nanodisk were obtained to construct various anisotropic Pt-Au heterostructures as plasmonic photocatalysts [101]. The Pt-edged Au O-TNP with larger tip area and electric field enhancement is beneficial for hot electron transfer and charge separation, resulting in higher efficiency in photocatalytic H_2 generation (Figs. 8g–i). To improve charge separation, reduced graphene oxide (rGO) with high conductivity was introduced to facilitate hot electrons transfer from plasmonic to catalytic metals. Ternary 2D Au-TNP/rGO/Pt nanoframe (NF) as plasmonic photocatalysts are preferable for boosting H_2 generation under vis-NIR light. The hot electrons generated on Au TNP are quickly transferred to rGO and further collected by loaded Pt NF cocatalyst, leading to efficient charge separation for high photocatalytic activity [102]. Recently, Huang *et al.* reported multimetallic heterostructure of Pd-dotted Ag@Au hexagonal nanoplates (HNPs), where plasmonic core-shell Ag@Au structure act as an ideal light absorber and Pd nanodots provide more catalytic active sites [103]. The heterostructure exhibits an excellent catalytic activity for formic acid (HCOOH) dehydrogenation even at 0 °C with turnover frequency of 1062 h^{-1}, due to plasmon-induced hot electron transfer from Ag@Au HNPs to Pd dots.

By analyzing the relaxation path, most hot carriers may undergo further thermalization *via* electron-phonon scattering and

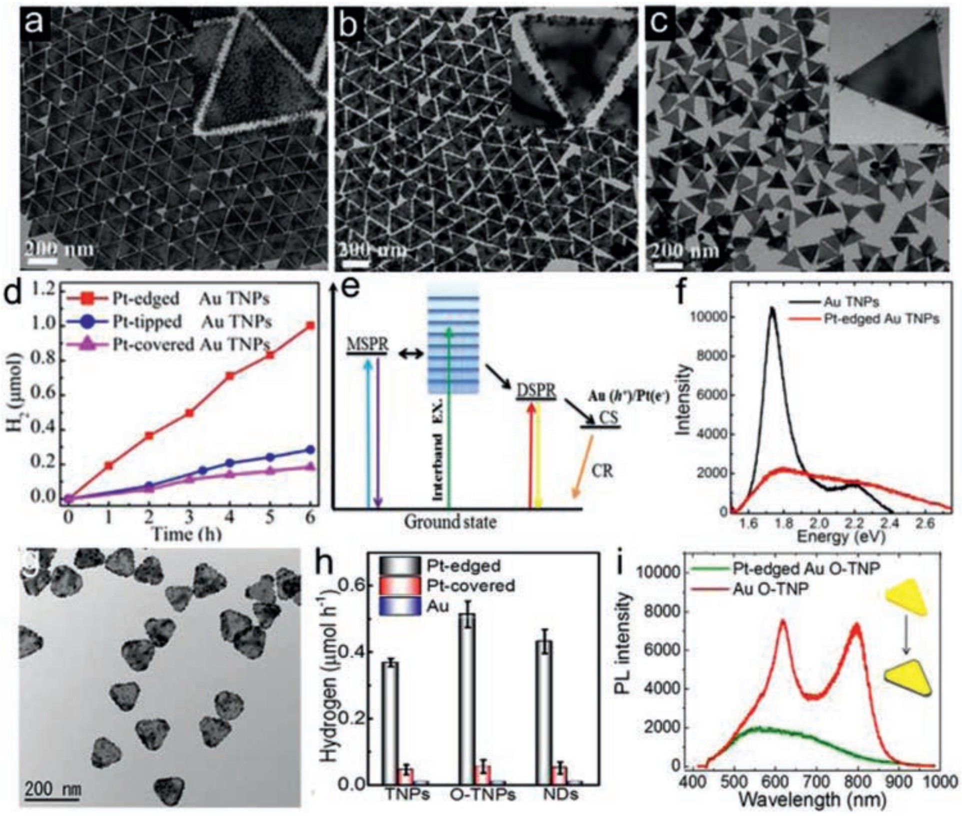

Fig. 8. TEM images of (a) Pt-covered, (b) Pt-edged and (c) Pt-tipped Au TNPs. (d) H_2 evolution over different photocatalysts. (e) Schematic diagram of plasmon radiative decay in Au TNPs. (f) Single-particle PL spectra. Reproduced with permission [100]. Copyright 2016, American Chemical Society. (g) TEM image, (h) H_2 generation rates and (i) Single-particle PL spectra of Pt-edged Au O-TNPs. Reproduced with permission [101]. Copyright 2017, American Chemical Society.

lead to photothermal heating, which is also an effective driving force for accelerating surface reaction. However, the two plasmonic effects of hot-electrons and photothermal conversion are usually entangled, making it hard to quantify their individual contribution to chemical reactions. To distinctly differentiate these two effects, Huang and co-workers reported a bar-shaped core-shell Au@Pd system toward Vis-NIR light-driven catalytic styrene hydrogenation, since that hot electrons have been considered as detrimental to hydrogenation [104]. Intriguingly, the Pd shell thickness could serve as a knob to maneuver the processes of hot-electron transfer and photothermal conversion, building a platform for unraveling their roles in catalytic reactions. As Pd shell thickness was tuned to 14 atomic layers precisely, photothermal heating efficiency was maximized while the side effect of plasmonic hot electrons was suppressed. Consequently, owing to plasmonic thermal effect, Au@Pd achieved high conversion yield of 76% in photocatalytic styrene hydrogenation to ethylbenzene, comparable to that achieved via thermally driven process at 80 °C. For most chemical reactions, both hot electrons and photothermal effect make positive contributions, synergistically enhance plasmonic catalytic efficiency.

There are several distinct features of hot carrier contribution to chemical reaction that can be used to experimentally differentiate from photothermal effect including: (1) Linear dependence of reaction rate on light intensity due to the fact that hot carrier generation rate increases linearly with photon flux [105], (2) a higher kinetic isotope effect or modified products selectivity in chemical reaction compared with that driven by thermal energy at same reaction temperature [106], (3) similar tendency of apparent quantum efficiency (AQE) with LSPR absorption spectrum of plasmonic NPs [73]. A clear separation of these two effects facilitates the rational design of plasmonic photocatalysts for efficient photochemical applications and solar energy utilization.

4. Nonmetallic materials as plasmonic photocatalysts

Recently, various nonmetallic nanomaterials have emerged as potential LSPR hosts and can be classified based on the origin of their LSPR properties. The ones that would be discussed in this review are heavily doped metal oxides (MoO_{3-x}, WO_{3-x}, NiO), metal chalcogenides ($Cu_{2-x}S$, $Cu_{2-x}Se$), and other semiconductors (TiN, Bi_2WO_6, BP) *etc.* We will highlight the development of these plasmonic semiconductors regarding on their synthesis methods and their promising applicability in plasmon enhanced photoredox catalysis such as H_2 evolution, CO_2 reduction, nitrogen reduction, pollution decomposition.

4.1. Plasmonic metal oxides

Plasmonic metal oxides with rich oxygen vacancies (OVs) have drawn tremendous interest in photocatalysis owing to their abundant reserve, facile synthetic method and good electrochemical stability. The OVs, basically a type of intrinsic defects, can serve as electron donor sites to modulate optical properties of a material [107]. Introduction of rich OVs is an effective strategy to increase free electrons density in semiconductors, inducing strong LSPR properties. In addition, OVs also facilitate charge transfer between semiconductor and adsorbed intermediates, thereby leading to enhanced photoredox reaction. Mostly reported metal oxides with OVs-induced LSPR are WO_{3-x} and MoO_{3-x}, which have been widely used for plasmonic photocatalysis.

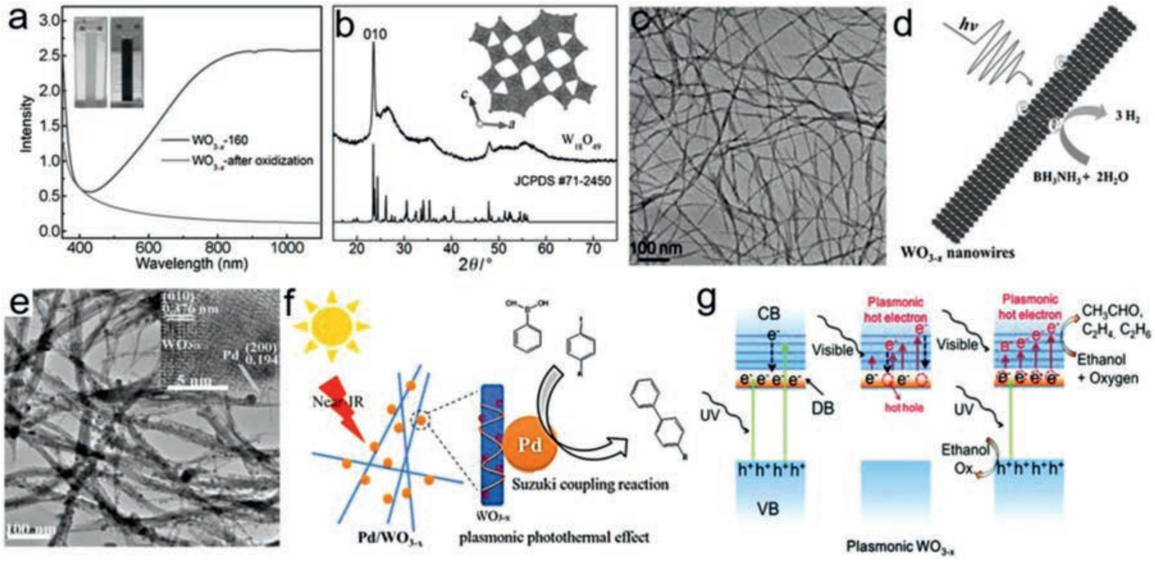

Fig. 9. (a) UV–Vis absorption spectra, (b) XRD patterns, (c) TEM image and (d) schematic photocatalytic H_2 evolution from ammonia borane over WO_{3-x} NWs. Reproduced with permission [112]. Copyright 2015, WILEY-VCH. (e) TEM image and (f) schematic photocatalytic Suzuki coupling reactions over Pd/WO_{3-x} NWs. Reproduced with permission [113]. Copyright 2015, Elsevier B.V. (g) Photoelectron and hot electron generation in self Z-scheme heterostructure of WO_{3-x} under UV-Vis irradiation. Reproduced with permission [114]. Copyright 2019, the Royal Society of Chemistry.

4.1.1. Tungsten trioxide

Tungsten trioxide (WO_{3-x}), an electrochromic material with suitable band gap of 2.6 eV, exhibits great potential in photocatalytic solar conversion. By removing oxygen atoms, disorder structure is formed in WO_3 lattice with large amounts of oxygen vacancies. The low valence state of W^{5+} are generated, forming different non-stoichiometric oxides such as $W_{20}O_{58}$, $W_{18}O_{49}$ and $W_{24}O_{68}$ [108]. With more introduction of OVs, the properties of WO_{3-x} are changed from semiconductor to metal, exhibiting strong LSPR in vis-NIR region. Various methods have been reported to synthesize WO_{3-x} with abundant OVs for enhanced photocatalysis. For instance, by annealing pristine WO_3 under H_2 atmosphere or vacuum at different high temperatures, WO_{3-x} samples with controlled OVs has been prepared successfully, displaying an improved photocurrent density [109,110]. Wang *et al.* tailored the amount and distribution of OVs on surface or bulk by tuning H_2 concentration during thermal treatment [111]. The amounts of bulk OVs on WO_3 monotonically rise with increasing of H_2 concentration, while that of surface OVs presents a volcano-type variation tendency. The WO_3 sample thermal-treated in 20% H_2 (WO_3-H_2O) contains the largest amount of surface OVs, which play more decisive role to achieve higher charge-carriers separation efficiency and photocatalytic O_2 evolution from water splitting.

One mostly used method to synthesize WO_{3-x} is simple surfactant-free solvothermal treatment. Lou *et al.* synthesized WO_{3-x} NWs via one-step solvothermal treatment using WCl_6 or $W(CO)_6$ as precursors and absolute ethanol as solvents. Owing to rich OVs on surface, WO_{3-x} NWs exhibit strong LSPR absorption in vis-NIR region and greatly promote H_2 generation from ammonia borane and Suzuki coupling reactions (Figs. 9a–f) [112,113]. Lou *et al.* found that under UV–vis irradiation, the unique electronic band structure of plasmonic WO_{3-x} can act as a self Z-scheme heterostructure (Fig. 9g). UV-excited photoelectrons are injected into conduction band of WO_{3-x}, stabilizing free electron density and accelerating plasmonic hot electron generation for photocatalytic ethanol dehydrogenation to aldehyde [114]. Moreover, both morphology and crystalline phase of WO_{3-x} were affected by species/concentration of precursors and solvents, temperature and time in solvothermal reaction [115]. Interestingly, NIR light excited plasmonic photothermal effect can make a big difference to the products selectivity. Under UV-vis-NIR irradiation, the synthesized WO_{3-x} NWs with abundant OVs selectively promote ethanol dehydration, yielding a remarkable ethylene generation rate of 16.9 mmol g^{-1} h^{-1}. Besides, plasmonic WO_{3-x} with thin amorphous surface was obtained using simple hydrochloric acid-assisted solvothermal method and also exhibits superior photocatalytic performance on CO_2 reduction reaction [116]. Intermediates detection indicates that the adjacent OVs around W^{4+} on amorphous surface of WO_{3-x} act as active sites for C–C coupling, leading to high-selective ethylene generation.

4.1.2. Molybdenum trioxide

Similar to WO_{3-x}, Molybdenum trioxide (MoO_{3-x}) is another reported metal oxide with OV-induced LSPR properties for solar-driven photocatalysis. Yamashita *et al.* firstly reported that plasmonic MoO_{3-x} nanosheets display an enhanced H_2 production from ammonia borane under visible light [40] (Figs. 10a–c). To date, plasmonic MoO_{3-x} has been successfully synthesized *via* liquid exfoliation approach, solvothermal method, soft template synthesis method, CO_2 assisted approach [117–121] *etc*. For example, Liu *et al.* reported to obtain amorphous plasmonic MoO_{3-x} nanosheets by MoS_2 oxidation and subsequent supercritical CO_2-treatment [117]. Etman *et al.* report the synthesis of MoO_{3-x} nanosheets *via* a liquid exfoliation approach to achieve efficient photocatalytic dye degradation [118]. Li *et al.* synthesized MoO_{3-x} nanobelts by a simple solvothermal method, which are utilized for photocatalytic N_2 fixation [119]. The surface OVs of MoO_{3-x} was found to chemisorb N_2 molecule and reduce its activation energy, playing a critical role in photocatalytic N_2 reduction to NH_3 (Figs. 10d–f). The obtained MoO_{3-x} *via* solvothermal method also exhibit high activity for photo-thermal synergistic CO_2 reduction under UV–vis-NIR irradiation. OVs-induced LSPR in MoO_{3-x} enables intense absorption in NIR region, leading to a strong thermal effect. Besides, OVs also improves CO_2 adsorption on the defective surface, decreases the barrier of CO_2 hydrogenation and carrier recombination during catalytic CO_2 conversion [121].

Apart from WO_{3-x} and MoO_{3-x}, Li group recently synthesized a new plasmonic semiconductor Bi_2O_{3-x} with rich OVs by oxidizing commercial bismuth powder in atmosphere at 453.15 K (Figs. 10g–i). The OVs induce LSPR in Bi_2O_{3-x} across the wavelength range of

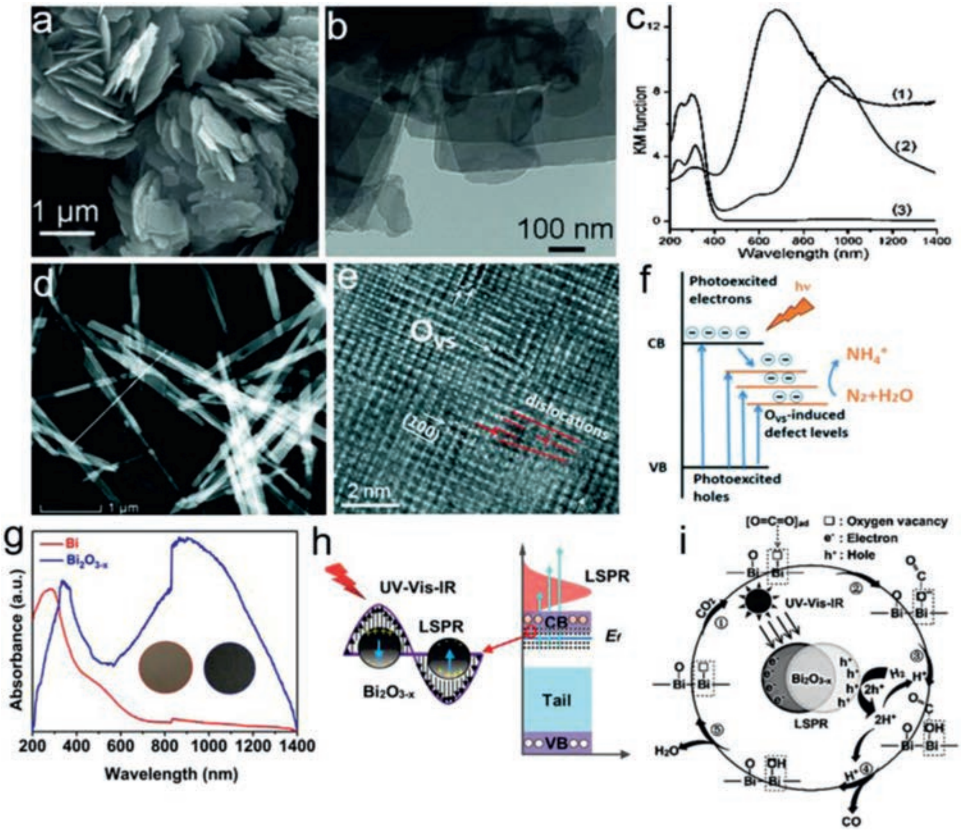

Fig. 10. (a) SEM image, (b) TEM image and (c) UV-vis-NIR DRS of MoO_{3-x} nanosheets. Reproduced with permission [40]. Copyright 2014, Wiley-VCH. (d) HAADF STEM image and (e) Atomic scale HAADF image showing ordered OVs in MoO_{3-x} nanobelts. (f) Electron transfer process during OVs-mediated N_2 fixation. Reproduced with permission [119]. Copyright 2019, the Royal Society of Chemistry. (g) Absorption spectra, (h) Schematic illustration of LSPR excitation and (i) possible pathway for photocatalytic CO_2 reduction over Bi_2O_{3-x}. Reproduced with permission [122]. Copyright 2020, Wiley-VCH.

600–1400 nm and enhance CO_2 molecules adsorption, which enable efficient photocatalytic CO_2 reduction to CO (100% selectivity) under low-intensity NIR irradiation. Similar to noble metals, the photocatalytic CO generation rate over Bi_2O_{3-x} shows a nearly linear dependence on light intensity and temperature, which suggests that catalytic performance originates from the synergetic effect between light irradiation and heating [122].

4.1.3. Other metal oxides

Nickel oxide (NiO) with superior electrochemical stability has been widely studied in photoelectrocatalysis. Nevertheless, as a p-type semiconductor with intrinsic hole doping and carrier self-trapping of amorphous nature, NiO NCs fail to act as individual photocatalyst to offer electrons for reduction reaction. Lin *et al.* reported 2D amorphous NiO nanostructure as a plasmonic photocatalyst for solar H_2 evolution without any cocatalysts [123]. They prepared 2D plasmonic amorphous NiO nanoflakes (2DPA) by laser ablation of bulk crystalline NiO powders in methanol solution. The 2D architecture can suppress the self-trapping induced carrier recombination and introduce LSPR property in NiO by increasing the electron doping. The solar H_2 evolution rate over 2DPA photocatalyst was improved by a factor of 19.4 owing to plasmon-mediated charge releasing. Another metal oxide indium oxide (In_2O_3) has also attracted interest for tunable LSPR that occurs in near- to mid-NIR region by aliovalent ion doping. Two plasmonic systems of Ti and Sb doped In_2O_3 NCs have been reported, which allow for a significant expansion and tunability of plasmon band [54]. By a self-assembly technique, In_2O_3 was encapsulated into bundled TiO_2 NW arrays, displaying broadband LSPR absorption of 84% in range of 400–2500 nm. This plasmonic photocatalyst achieved an improved catalytic activity for methyl orange degradation arising from LSPR effect of the In_2O_3 membrane, which extends light response and excites hot carriers [124].

4.1.4. Metal oxides heterostructures

The OVs are easily removed in aqueous solution, leading to unstable LSPR effect and decreased catalytic efficiency. In addition, excited hot electrons on the surface can react with the adsorbates and the associated free electron density decrease, which further weaken the LSPR effect and hot electron generation. To solve this problem, Lou *et al.* proposed the concept of electron injection to maintain free carrier density and stabilize LSPR effect of OVs-doped semiconductors by constructing heterostructures with other semiconductors [76]. Heterostructural CdS/WO_{3-x} NWs were synthesized by *in-situ* solvothermal growth of WO_{3-x} on CdS NWs, which exhibit superior activity than WO_{3-x} and CdS alone for photocatalytic H_2 generation. Single-particle PL study demonstrated that photogenerated electrons in CdS NWs are injected into conduction band of WO_{3-x}, which stabilizes its LSPR effect and boosts continuous hot electrons generation for efficient photocatalysis (Figs. 11a–c). Plasmonic heterostructure TiO_2-mesocrystals/WO_{3-x} NWs (TiO_2-MCs/WO_{3-x} NWs) were also constructed *via* a simple solvothermal procedure, and used for photocatalytic CO_2 reduction [125]. The obtained heterostructure exhibits much higher activity and selectivity (16.3 μmol g^{-1} h^{-1}, 83%) than TiO_2-MCs (3.5 μmol g^{-1} h^{-1}, 42%) and WO_{3-x} NWs (8.0 μmol g^{-1} h^{-1}, 64%) for CH_4 generation (Figs. 11d–f). The PL study demonstrates the photoelectron injection from TiO_2 to WO_{3-x} boosting hot electron generation, which plays a great role in highly selective CH_4 generation from CO_2 reduction. For efficient photoelectron injection, Li

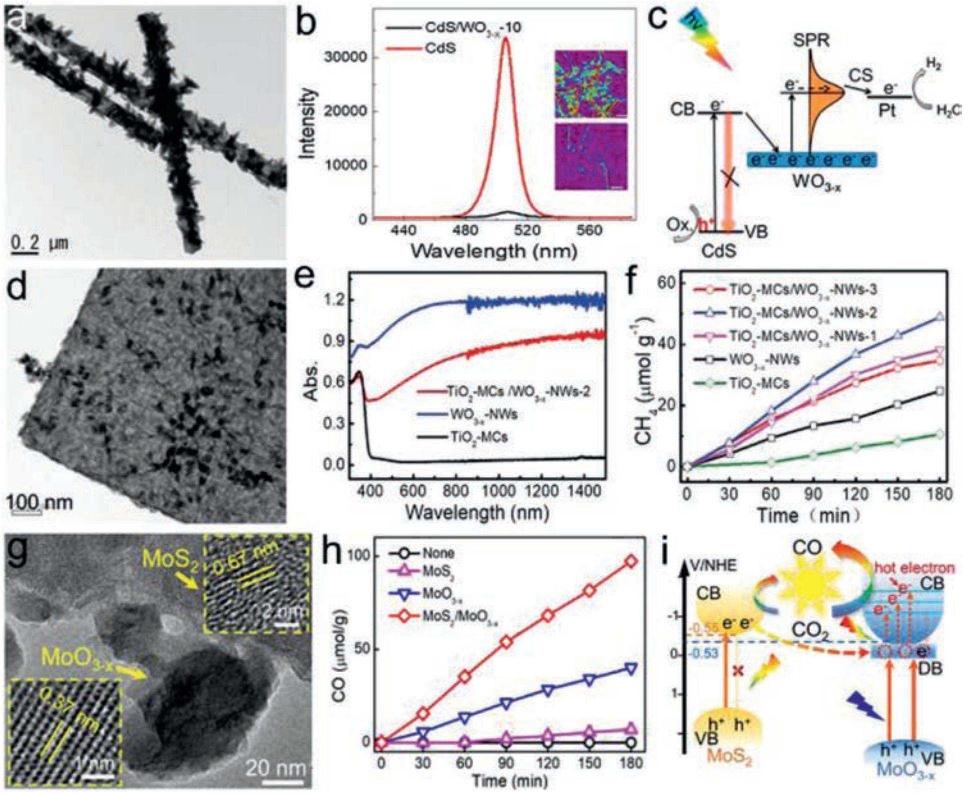

Fig. 11. (a) TEM image of CdS/WO_{3-x}. (b) Single-particle PL spectra and (c) schematic diagram showing the electrons injection from CdS to WO_{3-x}. Reproduced with permission [76]. Copyright 2017, Elsevier B.V. (d) STEM image of TiO_2-MCs/WO_{3-x} NWs. (e) Absorption spectra and (f) CH_4 evolution over the as-prepared photocatalysts. Reproduced with permission [125]. Copyright 2019, Wiley-VCH. (g) TEM images, (h) CO evolution and (i) excitation and electron transfer over MoS_2/MoO_{3-x} heterostructure. Reproduced with permission [127]. Copyright 2021, American Chemical Society.

et al. recently proposed to construct atom-sharing heterostructure of MoS_2/MoO_{3-x} with good interfacial contact via light-induced *in situ* partial oxidation of MoS_2 nanosheets [126]. The OVs induce intense LSPR of MoO_{3-x} and promote photoelectron injection from MoS_2 into MoO_{3-x}, leading to stable LSPR and continuous hot electron generation for enhanced photocatalysis. An enhanced CO generation rate of 32.4 μmol g^{-1} h^{-1} with high selectivity of 94.1% was achieved over the heterostructure under UV–vis-NIR irradiation (Figs. 11g–i). Wei group synthesized flexible $MoS_2@MoO_3$ core-shell nanowires with tunable plasmon resonance using a two-step method, realizing broadband light absorption and improved interfacial contact for better carrier transport [127]. The plasmonic $MoS_2@MoO_3$ exhibits good stability and flexibility in photocatalytic water splitting and yields an optimized H_2 evolution rate of 841.4 μmol h^{-1} g^{-1}.

Similar to metals, plasmon-induced hot electrons are expected to play great roles on promoting catalytic reaction. By constructing semiconductor heterostructures, LSPR effect can be stabilized *via* photogenerated carrier injection maintained free carrier concentration. However, currently reported semiconductor heterostructures still suffer from fast recombination of hot carriers, which hinders commercial application of plasmonic catalyst. Besides, single plasmonic semiconductor fail to meet the required potential to driven reduction reaction. A valid strategy to overcome these restrictions is to integrate plasmonic catalysts with appropriate active semiconductors for constructing a new generation of plasmonic heterostructures. Zhang *et al.* constructed a plasmonic Z-scheme photocatalyst by solvothermally integrating 1D plasmonic $W_{18}O_{49}$ nanograsses onto exfoliated 2D graphitic carbon nitride (g-C_3N_4) nanosheets [128]. The plasmon-excited hot electrons of $W_{18}O_{49}$ nanograsses can be injected into neighboring g-C_3N_4 that possesses abundant active sites and strong redox capacity, boosting long-lived hot electron generation for improved photocatalytic protons reduction. Almost a full-spectrum-driven H_2 evolution efficiently was achieved over $W_{18}O_{49}/g$-C_3N_4 heterostructure through the synergistic effect between Z-scheme charge-carriers separation and plasmon induced hot electrons injection (Figs. 12a and b). They also fabricated $W_{18}O_{49}/TiO_2$ branched heterostructure via solvothermal growth of plasmonic $W_{18}O_{49}$ NWs branches onto TiO_2 nanofiber backbones [129]. Using ultrafast transient absorption spectroscopy combined with FDTD simulations, plasmonic hot electrons were demonstrated to transfer from $W_{18}O_{49}$ branches to TiO_2 backbones within a very short timescale of 200 fs, much faster than the relaxation process (7–9 ps). Such an ultrafast transfer effectively improves the generation and separation of plasmonic hot electrons, thereby leading to an enhanced IR-driven catalytic activity for H_2 generation from ammonia borane (Figs. 12c and d). By pulsed laser deposition and plasma sputtering reaction deposition, plasmonic Z-scheme core-shell $W_{18}O_{49}/g$-C_3N_4 nanocone arrays were also successfully prepared to achieve more efficient plasmon-excited hot electron injection, spatial carriers separation and carrier lifetime extension [130]. Besides, Z-scheme heterostructure photocatalyst of $W_{18}O_{49}$/CdS was also synthesized by *in-situ* anchoring 0D $W_{18}O_{49}$ quantum dots on the surface of 1D CdS NRs [131]. Both bulk and surface photo-induced carriers are separated efficiently, achieving an improved photocatalytic H_2 evolution performance (Figs. 12e–g). A Z-scheme $BiO_{2-x}/Bi_2O_{2.75}$ heterostructure photocatalysts with rich OVs was prepared *via* a simple low-temperature hydrothermal method [132]. The Z-scheme interfacial heterojunction boosts the separation and migration of photoinduced charge carrier as well as improves the redox ability. Consequently, the as-prepared $BiO_{2-x}/Bi_2O_{2.75}$

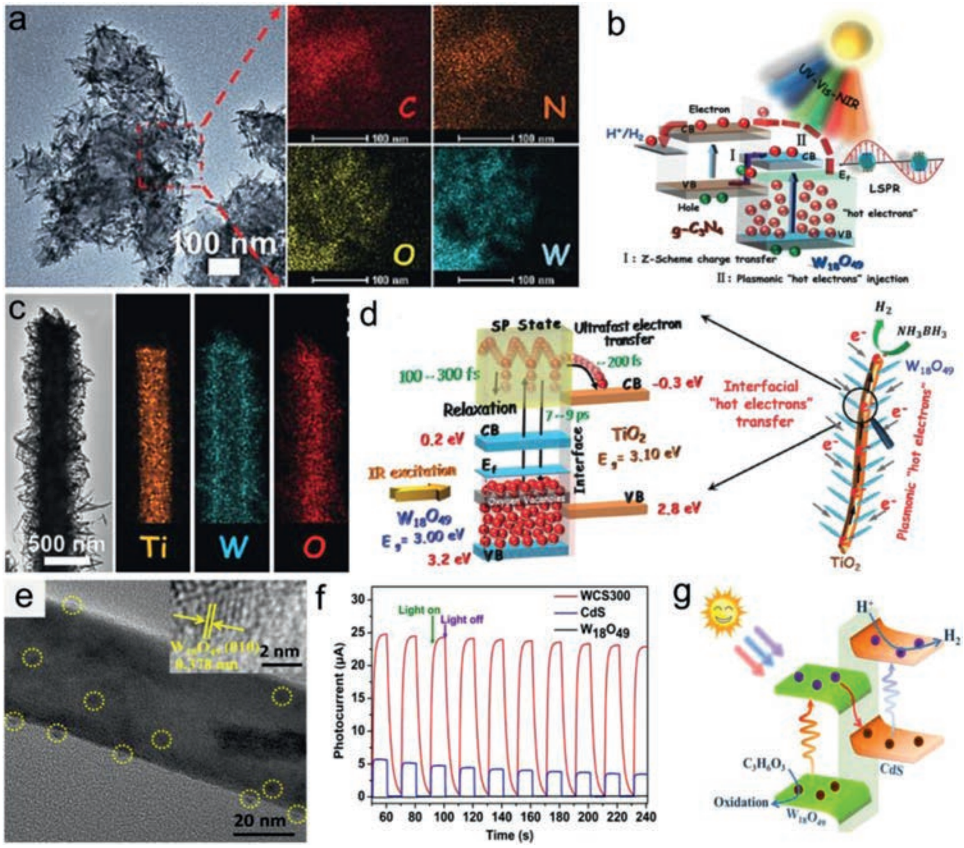

Fig. 12. (a) TEM and elemental mapping images, (b) energy band and photoinduced charge-carriers transfer process of $W_{18}O_{49}$/g-C_3N_4 heterostructure. Reproduced with permission [128]. Copyright 2017, Wiley-VCH. (c) TEM and corresponding elemental mapping images, (d) schematic kinetics process of plasmon hot electrons for H_2 generation from NH_3BH_3 over $W_{18}O_{49}/TiO_2$ branched heterostructure. Reproduced with permission [129]. Copyright 2018, Wiley-VCH. (e) TEM images of $W_{18}O_{49}$/CdS heterostructure and corresponding HRTEM image of (010) plane of $W_{18}O_{49}$ component (inset). (f) Transient photocurrent response and (g) Illustration of H_2 evolution mechanism over $W_{18}O_{49}$/CdS NRs. Reproduced with permission [131]. Copyright 2021, Elsevier B.V.

exhibits an enhanced photocatalytic activity in RhB degradation compared to pure BiO_{2-x}, ascribing to the synergistic effects of OVs-induced LSPR and Z-scheme heterogeneous interface. In addition to band alignment, steering an electron flow is of significance for developing efficient plasmonic catalysts. Wen *et al.* prepared plasmonic catalyst by coating ZIF-8 (zeolitic imidazolate frameworks) on plasmonic MoO_{3-x} surface and subsequent depositing Pd NPs on ZIF-8 (Pd/MoO_{3-x}@ZIF-8) [133]. Plasmon-induced hot electrons in MoO_{3-x} are injected into ZIF-8 and further transferred to Pd active sites through a Schottky junction, which greatly accelerating plasmon-induced electron transfer from MoO_{3-x} to Pd active sites. The heterostructure formed effectively retards the recombination of hot electron-hole pairs in MoO_{3-x}, leading to a higher catalytic activities for nitroaromatics hydrogenation.

4.2. Plasmonic metal chalcogenides

Metal chalcogenides with narrow bandgaps are one of potential candidates for photocatalytic applications. Similar to metal oxides, plasmonic property in chalcogenides also can be induced by introduction of vacancies. However, contrary to metal oxides, LSPR property in chalcogenides arises due to collective oscillation of cation vacancy-induced free holes in valence band (VB) rather than free electrons. Metal chalcogenides can be obtained by binding ligand-coordinated chalcogenide species to metal precursors. By changing metal-chalcogen ratios, tunable stoichiometric ratios and cation vacancies are achieved [52]. An emerging class of copper chalcogenide materials for plasmonic photocatalysis will be discussed in this section.

Self-doped copper chalcogenide ($Cu_{2-x}X$: X = S, Se, Te) have drawn great attention due to their LSPR absorption in NIR region, which is generated by the oscillation of Cu vacancy induced free holes. Various approaches have been reported to synthesize $Cu_{2-x}X$ with tunable crystal phase, stoichiometry and morphology, including solvothermal, hot-injection, wet chemical and templated method [134–138]. Shao *et al.* prepared a range of vacancy-doped $Cu_{2-x}S$ NCs ($Cu_{1.2}S$, $Cu_{1.4}S$, $Cu_{1.75}S$ and $Cu_{1.94}S$) with size of ~10 nm through a hot injection method [138]. By varying the injection volume of sulfur powder-oleic acid, the doping level of samples were manipulated to finely tune the LSPR wavelength. The obtained $Cu_{1.94}S$ NCs with the highest LSPR energy exhibited superior photocatalytic activity in dye degradation due to Cu vacancies induced high density of free holes. Gan *et al.* prepared $Cu_{2-x}Se$ NCs *via* a hot injection method and observed plasmon-driven chemical reaction of 4-nitrobenzenethiol dimerization on $Cu_{2-x}Se$ surfaces with considerable yields [136].

The $Cu_{2-x}X$-based heterostructures have attracted extensive attention because they can inhibit the photogenerated carriers recombination for improved photocatalysis. Plasmonic $Cu_{2-x}S$ nanodots were successfully deposited on two-dimensional (2D) g-C_3N_4 nanosheets by one-step hydrothermal growth method [139]. With efficient charge separation and strong light absorption, the 0D/2D plasmonic $Cu_{2-x}S$/g-C_3N_4 nanosheets achieved 100% degradation rate in 20 min for typical antibiotic pollutant, showing excellent catalytic degradation effect under UV–vis-NIR broad spectrum. Lian *et al.* synthesized CdS/Cu_7S_4 heterostructured NCs by a seeded growth reaction of disk-shaped Cu_7S_4 NCs and a subsequent partial cation exchange with Cd^{2+} [140]. The CdS/Cu_7S_4

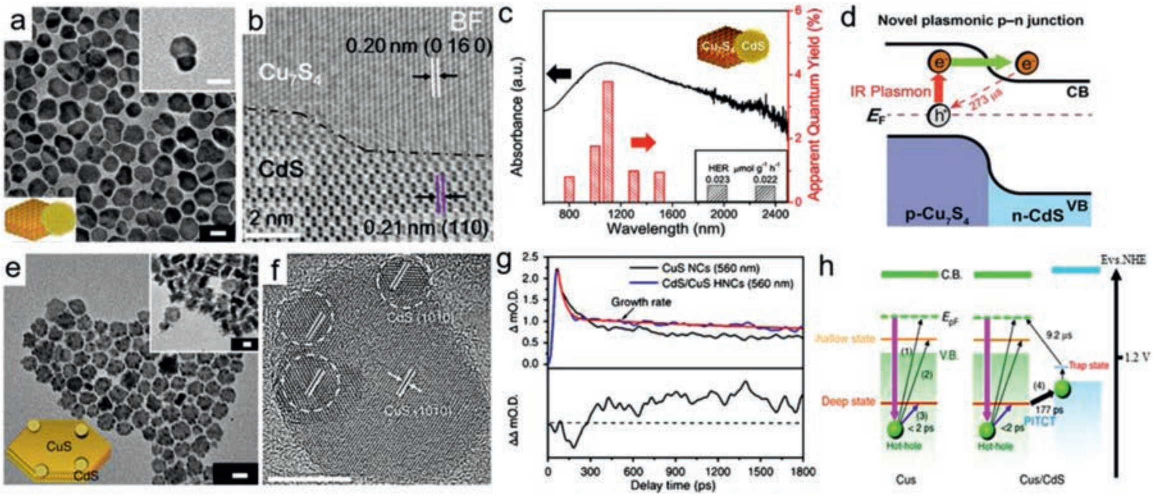

Fig. 13. (a) TEM image, (b) bright-field scanning TEM image and (c) absorption spectrum and AQY for H_2 evolution reaction over CdS/Cu_7S_4 HNCs. (d) Hot-electron injection of plasmonic p–n CdS/Cu_7S_4 HNCs upon IR light excitation. Reproduced with permission [140]. Copyright 2018, American Chemical Society. (e) TEM image and (f) HRTEM image of CdS/CuS HNCs. Scale bars: 10 nm. (g) Decay profiles of CuS and CdS/CuS HNCs at 560 nm, in which the rising part corresponds to the trapped holes of CdS in CdS/CuS HNCs. (h) Schematic illustration of LSPR-induced holes transfer [142]. Copyright 2018, Nature Publishing Group.

NCs achieved efficient photocatalytic H_2 evolution driven by near- to shortwave-IR light (up to 2500 nm) irradiation. The apparent quantum yield reached 3.8% at 1100 nm, which exceeds most IR-light energy conversion systems reported. Spectroscopic results revealed the plasmon-induced hot electron injection and long-lived charge separation ($>$ 273 μs) at p−n heterojunction of CdS/Cu_7S_4 NCs, which contributes to efficient IR light to hydrogen conversion (Figs. 13a–d). Moreover, a hollow sandwich-layered octahedral structure of $Cu_{2-x}S$/CdS/Bi_2S_3 with p−n−p type tandem heterojunctions was constructed via continuous growth deposition method [141]. This unique structure provides large surface area, rich reaction sites and improved separation and transfer of photogenerated carriers. Under Vis-NIR irradiation, $Cu_{2-x}S$/CdS/Bi_2S_3 as photocatalyst displays a high H_2 production rate (8012 μmol $h^{-1}g^{-1}$), and 2,4-dichlorophenol is almost degraded completely in 150 min. Though $Cu_{2-x}S$ primarily produce hot holes, the electrons of hot electron−hole pairs appear to be more active to drive chemical reactions in $Cu_{2-x}S$-based photocatalysts above, possibly due to the shorter lifetime of holes compared with electrons. From the kinetic perspective, it is difficult to achieve sufficient collection of hot holes for photocatalysis. Hot holes transfer has been proposed as a possible mechanism for contributing to photocatalytic activity by constructing heterostructured nanocrystals (HNCs) composed of plasmonic $Cu_{2-x}S$ and other semiconductors acting as acceptor. Lian *et al.* elucidate LSPR-induced hot holes transfer in CdS/CuS HNCs using time-resolved infrared (TR-IR) spectroscopy (Figs. 13e–h) [142]. The spectroscopic results provide an insight into a novel multi-step holes transfer mechanism named plasmon-induced transit carrier transfer (PITCT), in which the excited hot holes were not directly injected into CdS phase, but transferred stepwise through the carrier trapping state. Schematic decay processes of hot holes generated in CuS and CdS/CuS HNCs are shown in Fig. 13h. For single CuS, the generated hot holes decayed *via* phonon–hole scattering (1), hole trapping to the shallow state (2) or deep state (3), followed by relaxation to intrinsic hole state. For CdS/CuS HNCs, the holes in deep state transferred to VB of CdS (4, PITCT) and then the holes in CdS moved to trapping state, displaying structureless absorption in vis-region and recombination to the initial state. The PITCT of CdS/CuS HNCs realizes high quantum yield of 19% and longlived charge separation (9.2 μs), contributing to a superior oxidation catalytic activity for MB dye than those of CuS or CdS NCs alone under NIR irradiation.

4.3. Other plasmonic semiconductors

In addition to oxides and sulfides, transition metal nitrides (TMNs) is also a type of material with a significant prospect for extensive photocatalytic applications due to their distinct physical, electronic properties and metal-like properties. Recently, Cheng *et al.* systematically discussed and summarized different roles of TMNs materials in photocatalytic systems including semiconductor active components, co-catalysts, LSPR components, *etc* [143]. To date, TiN and WN have been applied for photocatalysis through LSPR effect, which is verified by both theoretical and experimental results. For example, plasmonic nanohybrid of plasmonic TiN nanocubes decorated with Pt NCs has been reported to efficiently drive H_2 evolution from NH_3BH_3 dehydrogenation. The apparent quantum yield reaches 120% under resonant light at 700 nm driven by hot electrons only. Under solar irradiation, the activity of TiN−Pt nanohybrids is enhanced by one order owing to the synergistic effect of plasmonic hot electrons and photothermal heating [84]. Heterostructures comprised of plasmonic TiN and other semiconductors have been proved to exhibit higher photocatalytic activity due to hot electron injection. Boltasseva *et al.* synthesized core–shell TiN@TiO_2 NPs with broad LSPR in red-NIR region. Under 700 nm fs-pulsed laser illumination, TiN@TiO_2 NPs effectively converts ground-state oxygen into singlet oxygen, driven primarily by hot electrons transferred from plasmonic TiN core to TiO_2 shell. Analytical calculations also reveal the unique advantages of TiN@TiO_2 heterostructures in hot-electron driven photocatalysis [144]. Another TMN of tungsten nitride (WN) with strong LSPR in NIR region has also been employed as photocatalyst for overall water splitting operated at red-light up to 765 nm [145]. Huang *et al.* proved the NIR-driven photocatalytic performance of plasmonic cubic-phase WN in effective reactive oxygen species activation by both density functional theory (DFT) calculation and experimental observation [146].

Apart from widely reported semiconductors above, several novel semiconductors with LSPR in vis-NIR region also have been developed as plasmonic photocatalysts. Lu *et al.* successfully constructed plasmonic Bi_2WO_6 with strong LSPR around 500–1500 nm region by electron doping [147]. Two types of OVs on W-O-W (V1) and Bi-O-Bi (V2) sites are precisely controlled by chemical methods, obtaining Bi_2WO_6-V1 with LSPR and Bi_2WO_6-V2 with defect absorption across Vis-NIR region separately. The DFT calculations

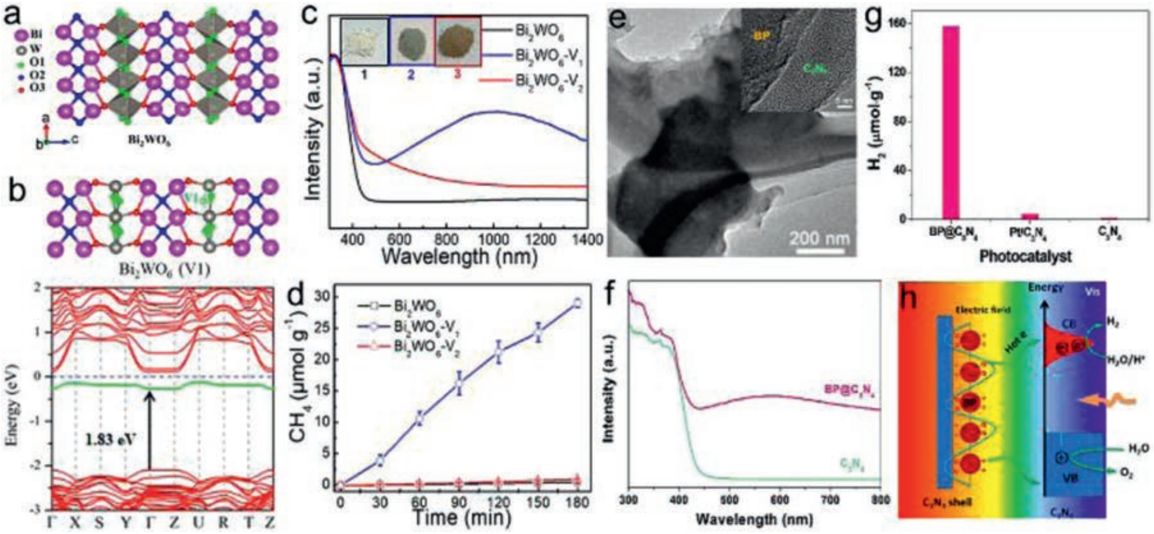

Fig. 14. (a) Crystal structure and (b) DFT-calculated band structure of Bi_2WO_6 with OVs on W-O-W sites. (c) UV-vis-NIR DRS with color images and (d) CH_4 generation over different Bi_2WO_6 samples. Reproduced with permission [147]. Copyright 2021, American Chemical Society. (e) TEM (HRTEM) images and (f) UV-vis absorption of $BP@C_3N_4$. (g) Photocatalytic H_2 generation and (h) proposed mechanism over metal-free plasmonic $BP@C_3N_4$ composite. Reproduced with permission [148]. Copyright 2021, Elsevier B.V.

indicate that V1 induced energy states have a small energy range of 0.25 eV and are close to conduction band, which facilitates photoelectron transfer and trapping for a long lifetime, leading to LSPR in Bi_2WO_6. A 93% PL quenching on Bi_2WO_6-V1 was observed by single-particle PL microscopy, demonstrating the photoelectron trapping on V1 sites. Plasmonic Bi_2WO_6-V1 boosts high-selective CH_4 generation with a rate of 9.95 μmol g^{-1} h^{-1} from photocatalytic CO_2 reduction, which is 26-fold higher than 0.37 μmol g^{-1} h^{-1} of Bi_2WO_6-V2 under UV–vis irradiation (Figs. 14a–d). Both DFT-simulation and *in situ* Fourier transform infrared spectra on Bi_2WO_6 surface prove that V1 sites facilitate CH_4 generation. The results imply the possibility of electron accumulations on the state to generate high carrier density and LSPR property. Introducing a doping electronic state to trap electrons is an effective strategy to modulate LSPR effect in semiconductors. Moreover, boron phosphide (BP) containing abundant III-V elements with strong covalent bonding exhibits indirect band gap of ~2.0 eV, excellent charge mobility and thermal stability (> 1000 °C), is potential to be a promising photocatalytic material [148,149]. Recently, Tian *et al.* reported a metal-free plasmonic core-shell BP@g-C_3N_4 photocatalyst with LSPR effect derived from free electrons collective oscillation on BP surface induced by abundant P-vacancies formed under high temperature [150]. The $BP@C_3N_4$ catalyst exhibits excellent solar energy utilization efficiency in UV–vis-NIR region and shows a remarkable photocatalytic activity for water splitting even under 730 nm illumination. The H_2 production rate can reach up to 31.5 μmol g^{-1} h^{-1} under visible light irradiation, which is 112.6 and 34.3 times higher than that of C_3N_4 and Pt/C_3N_4, respectively. The BP LSPR can facilitate generation and separation of charge carriers near the surface of C_3N_4, and plasmon-induced hot electrons transfer to CB of C_3N_4 for significantly improved water reduction reaction (Figs. 14e–h).

5. Conclusions and future prospects

Plasmonic photocatalysis has emerged as a promising technology to address the energy and environmental crisis. Owing to intriguing optical-electrical features such as intense light absorption, improved charge carrier separation, hot carriers generation and photothermal effect, plasmonic photocatalysts have effectively made their way to solar energy conversion applications including water splitting, CO_2 reduction, pollution decomposition *etc.* Although considerable progress has been made in plasmonic metal-based photocatalysts, high-cost and poor absorption in NIR region inhibited their large-scale practical applications, and also inspired the exploration of alternate plasmonic materials. Recently, heavily-doped semiconductors like nonstoichiometric oxides, sulfides, *etc.* have gained significant attention for the construction of LSPR with abundant oxygen/cation vacancies induced large free carrier density. By tuning the geometry and free carrier density, these semiconductors enable broadband solar energy harvesting across UV-vis-NIR range, highly desired for efficient photocatalysis. Even though recent efforts have been devoted to the development of novel plasmonic semiconductors for plasmon-driven photoredox reactions, there remain challenges accompanying them such as low utilization of hot carriers, obscure mechanism of hot carrier-driven reactions and unclear plasmon-related photochemical and physical process, *etc.* To realize full potential of plasmonic materials for development of efficient photocatalytic systems, prospective studies are still highly necessary towards the following regards.

5.1. Exploration of novel nonmetallic plasmonic materials

Heavily doped semiconductors exhibit great potential in photocatalysis due to their low cost, abundant reserve and strong LSPR in vis-NIR region. However, single plasmonic semiconductor still suffer from the low utilization of hot carriers, especially for hot hole in p-type semiconductors. Construction of asymmetric heterostructures of plasmonic and catalytic semiconductors with suitable potential position is an effective approach, where hot carrier transfer boosts long-lived hot carrier generation and separation for efficient photocatalysis. Besides, Milliron *et al.* discussed the presence of depletion layer near semiconductors surface that have a dramatically decreased free carrier density, largely damping LSPR effect. Therefore, developing plasmonic semiconductors with thin depletion layers is highly desirable, which also facilitates hot carriers separation for photocatalysis. Since the efficiency of plasmonic photocatalysts depends on geometry, configuration of plasmonic nanostructures should be specifically engineered with consideration of many design trade-offs. For example, 2D ordered plasmonic semiconductors or porous structure with distinct optical features, ease decoration and more active sites, might be a promising candidate for plasmonic photocatalysis. Generally, high-efficiency plasmonic photocatalysts possess features including stable LSPR effect, efficient charge carrier separation, suitable potential position and abundant active sites.

5.2. Uncover the mechanism of hot carrier-driven reactions

Plasmonic hot carriers have been demonstrated to play critical role in photocatalysis, but the underlying reaction mechanism still needs to be systematically studied. In contrast to progress of n-type plasmonic photocatalysts based on plasmon-induced hot electron transfer, there are few reports on hot holes transfer process regardless of its importance. The unclear behavior of hot holes remained an obstacle for the comprehensive understanding of hot carrier-drive reactions. An in-depth understanding of photochemical-physical process of hot carrier generation, transfer and recombination would clarify the role of hot carriers contributing the photocatalytic activity, and also beneficial to developing efficient plasmonic photocatalysts for high selectivity of anticipated products with zero side reactions. Recently, advanced experimental techniques including time-resolved infrared spectroscopy, single-particle PL spectroscopy, *etc.* have been employed to study the relaxation and transfer processes of hot carriers. However, there are still much processes left in fuzziness, and more techniques, especially the ones with high temporal-spatial resolutions, need to be introduced in research of plasmonic photocatalysis.

5.3. Insights into plasmon-related physicochemical process

Despite numerous efforts have been devoted to LSPR-driven catalytic reactions, there is still big room for the investigation of new processes, especially plasmonic photo-thermocatalysis. An insight into plasmon-related physicochemical processes should refer the knowledge from both plasmonic photocatalysis and photo-thermocatalysis to give a comprehensive description of the catalytic reactions. *In situ* characterization and temperature monitoring of plasmonic photocatalyst experimentally would be helpful to establish an in-depth understanding of detailed plasmon-related physicochemical process. Moreover, modeling and simulated studies could also be conducted to give insights into the underlying photocatalytic reaction mechanisms, such as thermal transfer, electronic transitions and interfacial charge transfer behaviors, which are expected to offer guideline for optimization of plasmonic photocatalysts.

Declaration of competing interest

The authors declare that they have no known competing financial interests or personal relationships that could have appeared to influence the work reported in this paper.

Acknowledgments

This work was supported by the National Natural Science Foundation of China (Nos. 11904133, 51872125), Guangdong Natural Science Funds for Distinguished Young Scholar (No. 2018B030306004) and GDUPS (2018), the Fundamental Research Funds for the Central Universities (No. 21619322) and Regional Joint Foundation in Guangdong Province (No. 2019A1515110210).

References

[1] R.C. Shen, D.D. Ren, Y.N. Ding, et al., Sci. China Mater. 63 (2020) 2153–2188.
[2] Q. Guo, C.Y. Zhou, Z.B. Ma, X.M. Yang, Adv. Mater. 31 (2019) 1901997.
[3] C.P. Xu, P.R. Anusuyadevi, C. Aymonier, et al., Chem. Soc. Rev. 48 (2019) 3868–3902.
[4] A. Fujishima, K. Honda, Nature 238 (1972) 37–38.
[5] S.J. Hu, M.S. Zhu, ChemCatChem 11 (2019) 6147–6165.
[6] H. Liu, Y.W. Feng, J.J. Shao, et al., Nano Energy 70 (2020) 104499.
[7] Y. Chen, M.J. Xu, J.Y. Wen, et al., Nat. Sustain. (2021), doi:10.1038/s41893-021-00697-4.
[8] P. Liao, M.C. Toroker, E.A. Carter, Nano Lett. 11 (2011) 1775–1781.
[9] L. Fu, R. Wang, C.X. Zhao, et al., Chem. Eng. J. 414 (2021) 128857.
[10] J.Z. Bloh, R. Dillert, D.W. Bahnemann, ChemCatChem 5 (2013) 774–778 Chaozheng Hea,d,1, Ran Wanga,1, Dan Xiangc.
[11] M.S. Zhu, C.Y. Zhai, S. Kim, et al., J. Phys. Chem. Lett. 10 (2019) 4017–4024.
[12] C.S. Vazquez, R.Q. Cabrera, M. Ling, et al., Adv. Funct. Mater. 27 (2017) 1605413.
[13] J.H. Yu, C.Z. He, C.Y. Pu, et al., Chin. Chem. Lett. (2021), doi:10.1016/j.cclet.2021.02.046.
[14] F. Naseem, P.L. Lu, J.P. Zeng, et al., ACS Nano 14 (2020) 7734–7759.
[15] G.C. Xi, S.X. Ouyang, P. Li, et al., Angew. Chem. Int. Ed. 51 (2012) 2395–2399.
[16] Z.Q. Liu, Z.Y. Lu, M. Bosman, et al., Small 14 (2018) 1803233.
[17] Y.Y. Gao, W. Nie, Q.H. Zhu, et al., Angew. Chem. 132 (2020) 18375–18380.
[18] S. Linic, P. Christopher, D.B. Ingram, Nat. Mater. 10 (2011) 911–921.
[19] B. Zeng, S.Y. Wang, Y.Y. Gao, et al., Adv. Funct. Mater. 31 (2021) 2005688.
[20] K. Awazu, M. Fujimaki, C. Rockstuhl, et al., J. Am. Chem. Soc. 130 (2008) 1676–1680.
[21] P. Wang, B. Huang, X. Qin, et al., Angew. Chem. Int. Ed. 47 (2008) 7931–7933.
[22] C. Tang, L.F. Liu, Y.L. Li, Z.F. Bian, Appl. Catal. B 201 (2017) 41–47.
[23] Y. Zhang, S. He, W. Guo, et al., Chem. Rev. 118 (2017) 2927–2954.
[24] J.S. DuChene, B.C. Sweeny, A.C. Johnston-Peck, et al., Angew. Chem. Int. Ed. 53 (2014) 7887–7891.
[25] M.J. Kale, T. Avanesian, P. Christopher, ACS Catal. 4 (2014) 116–128.
[26] W. Ahn, I. Vurgaftman, J.J. Pietron, et al., J. Mater. Chem. A 7 (2019) 7015–7024.
[27] X.G. Zhang, X.B. Ke, J.F. Yao, J. Mater. Chem. A 6 (2018) 1941–1966.
[28] X.G. Meng, L.Q. Liu, S.X. Ouyang, et al., Adv. Mater. 28 (2016) 6781–6803.
[29] Q. Chen, X.R. Cheng, H.M. Long, Y.F. Rao, Chin. Chem. Lett. 31 (2020) 2583–2590.
[30] S.Q. Luo, X.H. Ren, H.W. Lin, H. Song, J.H. Ye, Chem. Sci. 12 (2021) 5701–5719.
[31] W. Xua, H.C. Liu, D.L. Zhou, et al., Nano Today 33 (2020) 100892.
[32] J.M. Luther, P.K. Jain, T. Ewers, A.P. Alivisatos, Nat. Mater. 10 (2011) 361–366.
[33] S.W. Hsu, K. On, A.R. Tao, J. Am. Chem. Soc. 133 (2011) 19072–19075.
[34] Q.Q. Zhang, X.S. Li, Q. Ma, et al., Nat. Commun. 8 (2017) 14903.
[35] C.Y. He, H. Bai, W.C. Yi, et al., J. Mater. Chem. C 6 (2018) 3200–3205.
[36] J. Huang, J.W. Wang, Z.J. Hao, et al., Chin. Chem. Lett. 32 (2021) 3180–3184.
[37] W.X. Yang, Y.W. Liu, J.R. McBride, T.Q. Lian, Nano Lett. 21 (2021) 453–461.
[38] J. Li, W.N. Zhang, C.H. Lu, Z.Z. Lou, B.J. Li, Nanoscale Horiz. 4 (2019) 999–1005.
[39] K. Manthiram, A.P. Alivisatos, J. Am. Chem. Soc. 134 (2012) 3995–3998.
[40] H.F. Cheng, T. Kamegawa, K. Mori, H. Yamashita, Angew. Chem. 126 (2014) 2954–2958.
[41] H.F. Cheng, X.F. Qian, Y. Kuwahara, K. Mori, H. Yamamshita, Adv. Mater. 27 (2015) 4616–4621.
[42] X.C. Ma, Y. Dai, L. Yu, B.B. Huang, Sci. Rep. 4 (2014) 1–7.
[43] Q.W. Liu, Y.W. Wu, J.W. Zhang, et al., Appl. Surf. Sci. 490 (2019) 395–402.
[44] Y.Y. Li, C.Y. Zhong, M.X. Li, et al., J. Mater. Chem. C 9 (2021) 1614–1621.
[45] H.B. Tang, Z.H. Tang, J. Bright, et al., ACS Sustain. Chem. Eng. 9 (2021) 1500–1506.
[46] S. Kim, J.M. Kim, J.E. Park, J.M. Nam, Adv. Mater. 30 (2018) 1704528.
[47] H.J. Chen, L. Shao, Q. Li, J.F. Wang, Chem. Soc. Rev. 42 (2013) 2679–2724.
[48] M. Rycenga, C.M. Cobley, J. Zeng, et al., Chem. Rev. 111 (2011) 3669–3712.
[49] W.H. Li, Z.R. Guo, Q.Y. Tai, et al., Chin. Chem. Lett. 31 (2020) 2447–2451.
[50] M.A. Mahmoud, M. Chamanzar, A. Adibi, M.A. El-Sayed, J. Am. Chem. Soc. 134 (2012) 6434–6442.
[51] M.D. Lu, H. Zhu, L. Hong, et al., ACS Appl. Mater. Interfaces 12 (2020) 50929–50940.
[52] A. Agrawal, S.H. Cho, O. Zandi, et al., Chem. Rev. 118 (2018) 3121–3207.
[53] I. Kriegel, C.Y. Jiang, J. Rodríguez-Fernández, et al., J. Am. Chem. Soc. 134 (2012) 1583–1590.
[54] H.B. Fang, M. Hegde, P.H. Yin, P.V. Radovanovic, Chem. Mater. 29 (2017) 4970–4979.
[55] Y. Xie, A. Riedinger, M. Prato, et al., J. Am. Chem. Soc. 135 (2013) 17630–17637.
[56] D.X. Zhu, A.W. Tang, L. Peng, et al., J. Mater. Chem. C 4 (2016) 4880–4888.
[57] S.W. Hsu, W. Bryks, A.R. Tao, Chem. Mater. 24 (2012) 3765–3771.
[58] C. Clavero, Nat. Photonics 8 (2014) 95–103.
[59] X.C. Ma, Y. Dai, L. Yu, B.B. Huang, Sci. Appl. 5 (2016) e16017.
[60] Y.L. Li, Q. Sun, S. Zu, et al., Phys. Rev. Lett. 124 (2020) 163901.
[61] A. Manjavacas, J.G. Liu, V. Kulkarni, P. Nordlander, ACS Nano 8 (2014) 7630–7638.
[62] T.H. Tan, J. Scott, Y.H. Ng, et al., ACS Catal. 6 (2016) 1870–1879.
[63] Y.W. Liu, Q.L. Chen, D.A. Cullen, et al., Nano Lett. 20 (2020) 4322–4329.
[64] Y.H. Jang, Y.J. Jang, S. Kim, et al., Chem. Rev. 116 (2016) 14982–15034.
[65] N.Q. Wu, Nanoscale 10 (2018) 2679–2696.
[66] K. Qian, B.C. Sweeny, A.C.J. Peck, et al., J. Am. Chem. Soc. 136 (2014) 9842–9845.
[67] H. Song, X.G. Meng, Z.J. Wang, H.M. Liu, J.H. Ye, Joule 3 (2019) 1606–1636.
[68] M.J. Kale, P. Christopher, Science 349 (2015) 587–588.
[69] E. Cortés, Adv. Opt. Mater. 5 (2017) 1700191.
[70] L. Zhou, J.M.P. Martirez, J. Finzel, et al., Nat. Energy 5 (2020) 61–70.
[71] S. Zeng, E. Vahidzadeh, C.G. VanEssen, et al., Appl. Catal. B 267 (2020) 118644.
[72] J.W. Fu, K.X. Jiang, X.Q. Qiu, et al., Mater. Today 32 (2020) 222–243.
[73] H. Robatjazi, H. Zhao, D.F. Swearer, et al., Nat. Commun. 8 (2017) 1–10.

[74] J. Liu, J.W. Feng, J. Gui, et al., Nano Energy 48 (2018) 44–52.
[75] Z. Lou, S. Kim, M. Fujitsuka, et al., Adv. Funct. Mater. 28 (2018) 1706969.
[76] Z. Lou, M.S. Zhu, X.G. Yang, et al., Appl. Catal. B 226 (2018) 10–15.
[77] C.Y. Zhang, F.C. Jia, Z.Y. Li, X. Huang, G. Lu, Nano Res. 13 (2020) 3183–3197.
[78] Y. Dubi, I.W. Un, Y. Sivan, Chem. Sci. 11 (2020) 5017.
[79] Y. Liu, Z.Y. Zhang, Y.R. Fang, et al., Appl. Catal. B 252 (2019) 164–173.
[80] Z.J. Xie, Y.H. Duo, Z.T. Lin, et al., Adv. Sci. 7 (2020) 1902236.
[81] Z.J. Wang, H. Song, H. Liu, J.H Ye, Angew. Chem. Int. Ed. 59 (2020) 8016–8035.
[82] M. Ghoussoub, M.K. Xia, P.N. Duchesne, D. Segal, G. Ozin, Energy Environ. Sci. 12 (2019) 1122–1142.
[83] D. Mateo, J.L. Cerrillo, S. Durini, J. Gascon, Chem. Soc. Rev. 50 (2021) 2173–2210.
[84] S. Rej, L. Mascaretti, E.Y. Santiago, et al., ACS Catal. 10 (2020) 5261–5271.
[85] L. Zhou, D.F. Swearer, C. Zhang, et al., Science 362 (2018) 69–72.
[86] S.Q. Luo, H. Song, D. Philo, et al., Appl. Catal. B 272 (2020) 118965.
[87] M.Q. Sun, X.Q. Fu, K.X. Chen, H. Wang, ACS Appl. Mater. Interfaces 12 (2020) 46146–46161.
[88] L.Q. Liu, S.X. Ouyang, J.H. Ye, Angew. Chem. 125 (2013) 6821–6825.
[89] C. Han, Q. Quan, H.M. Chen, Y.G. Sun, Y.J. Xu, Small 13 (2017) 1602947.
[90] Z.F. Bian, T. Tachikawa, P. Zhang, M. Fujitsuka, T. Majima, J. Am. Chem. Soc. 136 (2014) 458–465.
[91] J.N. Shen, Z.Y. Chen, S.T. Han, et al., ChemCatChem 12 (2020) 2989–2994.
[92] B.D. Clark, C.R. Jacobson, M.H. Lou, et al., ACS Nano 13 (2019) 9682–9691.
[93] L. Yuan, M.H. Lou, B.D. Clark, et al., ACS Nano 14 (2020) 12054–12063.
[94] Z.K. Zheng, T. Tachikawa, T. Majima, J. Am. Chem. Soc. 136 (2014) 6870–6873.
[95] Z. Zheng, T. Tachikawa, T. Majima, J. Am. Chem. Soc. 137 (2015) 948–957.
[96] M. Hajfathalian, K.D. Gilroy, A. Yaghoubzade, et al., J. Phys. Chem. C 119 (2015) 17308–17315.
[97] X.Z. Zhu, H.L. Jia, X.M. Zhu, et al., Adv. Funct. Mater. 27 (2017) 1700016.
[98] K. Sytwu, M. Vadai, J.A. Dionne, Adv. Phys. X 4 (2019) 1619480.
[99] J. Guo, Y. Zhang, L. Shi, et al., J. Am. Chem. Soc. 139 (2017) 17964–17972.
[100] Z.Z. Lou, M. Fujitsuka, T. Majima, ACS Nano 10 (2016) 6299–6305.
[101] Z.Z. Lou, S. Kim, P. Zhang, et al., ACS Nano 11 (2017) 968–974.
[102] Z.Z. Lou, M. Fujitsuka, T. Majima, J. Phys. Chem. Lett. 8 (2017) 844–849.
[103] F.X. Tong, Z.Z. Lou, X.Z. Liang, et al., Appl. Catal. B 277 (2020) 119226.
[104] H. Huang, L. Zhang, Z. Lv, et al., J. Am. Chem. Soc. 138 (2016) 6822–6828.
[105] G. Baffou, I. Bordacchini, A. Baldi, R. Quidant, Light Sci. Appl. 9 (2020) 108.
[106] M. Bonn, S. Funk, C. Hess, et al., Science 285 (1999) 1042–1045.
[107] D. Zu, H.Y. Wang, S. Lin, et al., Nano Res. 12 (2019) 2150–2163.
[108] C. Bhattacharya, S.E. Saji, A. Mohan, et al., Adv. Energy Mater. 10 (2020) 2002402.
[109] Q. Liu, F.J. Wang, H.X. Lin, et al., Catal. Sci. Technol. 8 (2018) 4399–4406.
[110] L. Liang, X.D. Li, Y.F. Sun, et al., Joule 2 (2018) 1004–1016.
[111] Y.T. Wang, J.M. Cai, M.Q. Wu, et al., Appl. Catal. B 239 (2018) 398–407.
[112] Z.Z. Lou, Q. Gu, L. Xu, Y.S. Liao, C. Xue, Chem. Asian J. 10 (2015) 1291–1294.
[113] Z.Z. Lou, Q. Gu, Y.S. Liao, S. Yu, C. Xue, Appl. Catal. B 184 (2016) 258–263.
[114] C.H. Lu, J. Li, G.Y. Chen, B.J. Li, Z.Z. Lou, Nanoscale 11 (2019) 12774–12780.
[115] J. Li, G.Y. Chen, J.H. Yan, et al., Appl. Catal. B 264 (2020) 118517.
[116] C.H. Lu, J. Li, J.H. Yan, et al., Appl. Mater. Today 20 (2020) 100744.
[117] W. Liu, Q. Xu, W.L. Cui, C.H. Zhu, Y.H. Qi, Angew. Chem. Int. Ed. 56 (2017) 1600–1604.
[118] A.S. Etman, H.N. Abdelhamid, Y.Y. Yuan, et al., ACS Omega 3 (2018) 2193–2201.
[119] Y.H. Li, X. Chen, M.J. Zhang, et al., Catal. Sci. Technol. 9 (2019) 803–810.
[120] Z. Luo, R. Miao, T.D. Huan, et al., Adv. Energy Mater. 6 (2016) 1600528.
[121] J. Li, Y.H. Ye, L.Q. Ye, et al., J. Mater. Chem. A 7 (2019) 2821–2830.
[122] Y.X. Li, M.M. Wen, Y. Wang, et al., Angew. Chem. Int. Ed. 60 (2021) 910–916.
[123] Z.Y. Lin, C. Du, B. Yan, C.X. Wang, G.W. Yang, Nat. Commun. 9 (2018) 4036.
[124] H. Huang, Q. Hao, X.C. Fan, et al., Phys. Chem. Chem. Phys. 19 (2017) 27059–27064.
[125] Z.Z. Lou, P. Zhang, J. Li, et al., Adv. Funct. Mater. 29 (2019) 1808696.
[126] J. Li, X.H. Xu, B.B. Huang, Z.Z. Lou, B.J. Li, ACS Appl. Mater. Interfaces 13 (2021) 10047–10053.
[127] S.H. Guo, X.H. Li, X.G. Ren, et al., Adv. Funct. Mater. 28 (2018) 1802567.
[128] Z.Y. Zhang, J.D. Huang, Y.R. Fang, et al., Adv. Mater. 29 (2017) 1606688.
[129] Z.Y. Zhang, X.Y. Jiang, B.K. Liu, et al., Adv. Mater. 30 (2018) 1705221.
[130] P.X. Du, Y.N. Wei, J. Sun, et al., Phys. Chem. 125 (2021) 4205–4210.
[131] B. Wang, C.X. Chen, Y.Y. Jiang, et al., Chem. Eng. J. 412 (2021) 128690.
[132] M. Wang, G.Q. Tan, D. Zhang, et al., Appl. Catal. B 254 (2019) 98–112.
[133] M.C. Wen, S.N. Song, Q.X. Liu, et al., Appl. Catal. B 282 (2021) 119511.
[134] T.M. Mattox, X.C. Ye, K. Manthiram, et al., Adv. Mater. 27 (2015) 5830–5837.
[135] F.J. Tao, Y.L. Zhang, F.H. Zhang, et al., RSC Adv. 6 (2016) 63820–63826.
[136] X.Y. Gan, E.L. Keller, C.L. Warkentin, et al., Nano Lett. 19 (2019) 2384–2388.
[137] Y.C. Jiang, S.D. Zhang, Q. Ji, et al., J. Mater. Chem. A 2 (2014) 4574–4579.
[138] X. Shao, T.Y. Zhang, B. Li, et al., CrystEngComm 22 (2020) 678–685.
[139] L. Zhou, Z.H. Liu, Z.P. Guan, et al., Appl. Catal. B 263 (2020) 118326.
[140] Z.C. Lian, M. Sakamoto, J.J. Vequizo, et al., J. Am. Chem. Soc. 141 (2018) 2446–2450.
[141] M.J. Guo, T.Y. Zhao, Z.P. Xing, et al., ACS Appl. Mater. Interfaces 12 (2020) 40328–40338.
[142] Z.C. Lian, M. Sakamoto, H. Matsunaga, et al., Nat. Commun. 9 (2018) 2314.
[143] Z.X. Cheng, W.L. Qi, C.H. Pang, et al., Adv. Funct. Mater. 31 (2021) 2100553.
[144] X.H. Xu, A. Dutta, J. Khurgin, et al., Laser Photonics Rev 14 (2020) 1900376.
[145] Y.L. Wang, T. Nie, Y.H. Li, et al., Angew. Chem. 129 (2017) 7538–7542.
[146] W.C. Huang, Y. Gao, J.X. Wang, et al., Small 16 (2020) 2004557.
[147] C.H. Lu, X.R. Li, Q. Wu, et al., ACS Nano 15 (2021) 3529–3539.
[148] M.S. Zhu, S. Kim, L. Mao, et al., J. Am. Chem. Soc. 139 (2017) 13234–13242.
[149] X.D. Wang, J. He, J.Y. Li, et al., Appl. Catal. B 277 (2020) 119230.
[150] B. Tian, Y.Q. Wu, G.X. Lu, Appl. Catal. B 280 (2021) 119410.